



# Understanding the synergistic effect of hydrated electron generation from argon plasma catalysis over Bi<sub>2</sub>O<sub>3</sub>/CeO<sub>2</sub> for perfluorooctanoic acid dehalogenation: Mechanism and DFT study

Choe Earn Choong<sup>a,b</sup>, Minhee Kim<sup>c</sup>, Jun Sup Lim<sup>b</sup>, Young June Hong<sup>b</sup>, Geon Joon Lee<sup>b</sup>, Keun Hwa Chae<sup>d</sup>, In Wook Nah<sup>e</sup>, Yeomin Yoon<sup>f</sup>, Eun Ha Choi<sup>b</sup>, Min Jang<sup>a,b,\*</sup>

<sup>a</sup> Department of Environmental Engineering, Kwangwoon University, Seoul 01897, Republic of Korea

<sup>b</sup> Plasma Bioscience Research Center/Department of Electrical and Biological Physics, Kwangwoon University, Seoul 01897, Republic of Korea

<sup>c</sup> Ministry of Environment, 229 Misagangbyeonhangang-ro, Hanam-si, Gyeonggi-do 12902, Republic of Korea

<sup>d</sup> Advanced Analysis Center, Korea Institute of Science and Technology (KIST), Seoul 02792, Republic of Korea

<sup>e</sup> Center for Energy Convergence, Korea Institute of Science & Technology (KIST), 5, Hwarang-ro 14-gil, Seongbuk-gu, Seoul 02792 Republic of Korea

<sup>f</sup> Department of Environmental Science and Engineering, Ewha Womans University, 52 Ewhayeodae-gil, Seodaemun-gu, Seoul 03760, Republic of Korea

## ARTICLE INFO

### Keywords:

Plasma-catalysis  
Perfluorooctanoic acid  
Hydrated electrons  
Reactive oxygen species  
Pseudo-photocatalysis

## ABSTRACT

Pseudo-photocatalysis driven by argon-plasma-system (AP) is a new approach toward the promotion of reactive species production for water remediation. Here, we investigated the synergistic effect between AP and catalyst by altering the oxygen vacancies (O<sub>v</sub>) concentration of CeO<sub>2</sub>/Bi<sub>2</sub>O<sub>3</sub> for stimulating the hydrated electrons (e<sub>aq</sub><sup>-</sup>) production for PFOA removal. The soft X-ray total fluorescence yield (TFY) analysis and DFT calculation revealed the formation of the built-in electric field in the Bi/Ce<sub>0.43</sub> interface can enhance interfacial electron migration with direction from Bi<sub>2</sub>O<sub>3</sub> toward CeO<sub>2</sub>, simultaneously promoting the e<sub>aq</sub><sup>-</sup> generation. Notably, AP-Bi/Ce<sub>0.43</sub> (0.1488 min<sup>-1</sup>, E<sub>EO</sub> = 0.43 kW mg<sup>-1</sup>) exhibited excellent PFOA removal kinetic performance with almost 5.7 times faster and 72.6% lower energy consumption than sole AP (0.0261 min<sup>-1</sup>, E<sub>EO</sub> = 1.57 kW mg<sup>-1</sup>), respectively. The multiple-plasma-jet continuous-flow-experiments results illustrated the scalability of AP-Bi/Ce<sub>0.43</sub> for PFOA destruction. Our findings demonstrate fundamental insights into the synergistic effect of PFOA removal in AP catalysis.

## 1. Introduction

The perfluorooctanoic acid (PFOA) levels in the drinking water supplies for nearly 6 million US residents exceed the US Environmental Protection Agency (EPA) drinking water advisory level, which limits the cumulative or individual content of PFOA and PFOS to 70 ng L<sup>-1</sup> [1]. Generally, the PFOA is widely used to produce coating reagents, surfactants, and fire retardants. It is classified as a carcinogen and exhibits different degrees of toxicity in humans, including immunotoxicity and neurotoxicity [2]. In particular, PFOA contains a high C-F bond energy (~116 kcal mol<sup>-1</sup>) and is very stable in water bodies, thus complicating defluorination by conventional treatment technologies. The urgency of the pollution crisis and stringent regulation of PFOA necessitates the development of effective treatment methods.

Among all the water treatment technologies, plasma has been widely

investigated as a promising technology for the destruction of organic compounds [3] and disinfection [4]. Previous studies found that reactive species, including free electrons, hydrated electrons (e<sub>aq</sub><sup>-</sup>), and hydrogen radicals (·H), play a significant role in PFOA removal using a plasma system [5]. However, these reactive species have short decay times and low mass transfer from the gas to the liquid phase under Ar plasma (AP). Therefore, the effective creation of a high amount of reactive species in the liquid phase of AP could significantly boost PFOA removal performance. Generally, the UV or visible (VIS) range light, high-energy electrons, and reactive species can be produced simultaneously in plasma. In particular, the UV~VIS range light and electron collision energies (1–25 eV) produced from the plasma can fulfill the activation energy requirements for the semiconductor, thus yielding activated electrons (e<sup>-</sup>) and holes (h<sup>+</sup>) [6]. Therefore, the utilization of photocatalysts in AP (AP catalysts) could yield a high amount of e<sub>aq</sub><sup>-</sup> and

\* Corresponding author at: Department of Environmental Engineering, Kwangwoon University, Seoul 01897, Republic of Korea.

E-mail addresses: [minjang@kw.ac.kr](mailto:minjang@kw.ac.kr), [heejaejang@gmail.com](mailto:heejaejang@gmail.com) (M. Jang).

<https://doi.org/10.1016/j.apcatb.2023.123403>

Received 1 August 2023; Received in revised form 3 October 2023; Accepted 16 October 2023

Available online 19 October 2023

0926-3373/© 2023 Elsevier B.V. All rights reserved.

reactive oxygen species (ROS) via pseudo-photocatalysis, eventually increasing PFOA removal efficiency. Studies on AP catalysts for activating pseudo-photocatalysis are scarce, and the relationship between PFOA removal performance and the  $e_{aq}^-$  produced from AP is poorly understood. Therefore, it is significant to understand the efficient production of  $e_{aq}^-$  via AP catalysts.

Bismuth (Bi)-based materials have been extensively investigated in electrocatalysis, photocatalysis, and sonocatalysis due to their low toxicity and high reactivity in catalysis [7]. However, the low light energy utilization efficiency and high  $e^-/h^+$  recombination properties of Bi-based catalysts limit their application in photocatalysis [8]. Accordingly, heterojunction construction with a built-in electric field can improve the charge transfer and maximal carrier separation in Bi-based catalysts, thereby improving the photocatalytic performance [9]. Cerium oxide ( $CeO_2$ ) with a fluorite structure is an interesting catalyst owing to its 4 *f* orbital nonstoichiometric oxygen deficiency and reversible transformation capability between Ce(III) and Ce(IV) [10]. Composite between  $Bi_2O_3/CeO_2$  could introduce oxide-ion vacancies to balance charge and unsymmetrical coordination environment that may introduce structural distortion, enhancing catalytic properties. Therefore, we speculate that the introduction of unsymmetrical coordination of  $Bi_2O_3/CeO_2$  could be activated under AP, improving the  $e_{aq}^-$  generation.

In this study, we aimed to construct a novel design of  $Bi_2O_3/CeO_2$  (Bi/Ce) heterojunction catalysts with tunable oxygen vacancies ( $O_V$ ) interfaces. The characterization results showed the different concentration of  $O_V$  of  $Bi_2O_3/CeO_2$  was successfully prepared with distorted structure. As a result, the optimized catalyst was found to be 30% of  $CeO_2$  incorporated with  $Bi_2O_3$  (Bi/ $Ce_{0.43}$ ), forming  $O_V$  contained interface and improving the charge transfer efficiencies. As a result, this approach stimulated the  $e_{aq}^-$  production under AP assisted catalysis (AP catalysis). The combination of experimental and DFT calculation revealed that the photoexcited electron migrates from  $Bi_2O_3$  toward  $CeO_2$ , attributing to the formation of the built-in electric field in the catalyst interface. Accordingly, AP-Bi/ $Ce_{0.43}$  ( $0.1488 \text{ min}^{-1}$ ,  $E_{EO} = 0.43 \text{ kW mg}^{-1}$ ) achieved remarkable PFOA removal kinetic performance with approximately 5.7 times faster and 72.6% lower energy consumption than AP ( $0.0261 \text{ min}^{-1}$ ,  $E_{EO} = 1.57 \text{ kW mg}^{-1}$ ), respectively. Notably, continuous flow experiments (CFEs) using three AP jets with Bi/ $Ce_{0.43}$  coated glass beads (G-AP-Bi/ $Ce_{0.43}$ ) were performed to investigate the applicability of the AP catalyst for removing low-level PFOA. LC-MS-MS analysis showed that Bi/ $Ce_{0.43}$  suppressed the formation of PFOA by-products in AP owing to its high production of  $e_{aq}^-$  and hydroxyl radicals. This finding demonstrates a novel approach for the enhancement of the interfacial charge transfer effect in heterojunction catalysts in AP-induced pseudo-photocatalysis for improving  $e_{aq}^-$  production.

## 2. Materials and methods

### 2.1. Chemicals and reagents

Cerium nitrate [ $Ce(NO_3)_3$ ], bismuth nitrate pentahydrate [ $Bi(NO_3)_3 \cdot 5 H_2O$ ], 1,4-benzoquinone, sodium oxalate ( $Na_2C_2O_4$ ), tert-butyl alcohol, sodium sulfate ( $Na_2SO_4$ ), sodium chloride ( $NaCl$ ), ammonia solution ( $NH_4OH$ , 30%), hydrochloric acid ( $HCl$ ), sodium hydroxide ( $NaOH$ ), and silver nitrate ( $AgNO_3$ ) were obtained from Dae Jung Chemical, South Korea. 5,5-Dimethyl-1-pyrroline-N-oxide (DMPO) was obtained from Dojindo Molecular Technologies, Inc. (Japan). Methanol and PFOA were purchased from Sigma-Aldrich. All chemicals were of analytical grade and were used without further purification. PFAS mixtures containing five perfluoroalkyl carboxylic acids (PFCAs) [perfluorobutanoic acid (PFBA), perfluoropentanoic acid (PFPA), perfluorohexanoic acid (PFHxA), perfluoroheptanoic acid (PFHpA), and perfluorooctanoic acid (PFOA)] were obtained from Wellington Laboratories Inc. (Guelph, ON, Canada). Stable isotope labeled PFCA internal standard (SIL-IS) was purchased from Wellington Laboratories in  $2 \mu\text{g}$

$\text{mL}^{-1}$  solution mixtures (Guelph, ON, Canada):  $^{13}C_4$ -PFBA,  $^{13}C_2$ -PFHxA, and  $^{13}C_4$ -PFOA.

### 2.2. Preparation of catalysts

The AP catalysts,  $Bi_2O_3$ ,  $CeO_2$ , and Bi/Ce, were prepared by co-precipitation followed by calcination [11]. Various Bi/ $Ce_x$ , where *x* indicates the weight ratio of Ce to Bi, were prepared to investigate the optimum ratio between Ce and Bi for AP catalysis. Incorporation ratios of 10%, 20%, 30%, and 50% were designated as Bi/ $Ce_{0.11}$ , Bi/ $Ce_{0.25}$ , Bi/ $Ce_{0.43}$ , and Bi/ $Ce_{1.0}$ , respectively. Briefly, the Bi(III) and Ce(III) solutions were mixed by vigorous stirring for 30 min. Subsequently,  $NH_4OH$  was added to adjust the pH of the solution to 10. A dark yellowish solid was obtained and filtered using a  $0.45\text{-}\mu\text{m}$  pore Whatman filter paper. The filtered solid was transferred to an alumina crucible and heated in a muffle furnace at  $600^\circ\text{C}$  for 6 h in air. Finally, the obtained solid was pulverized into a fine powder using a mortar and pestle. Pure  $Bi_2O_3$  and  $CeO_2$  were also prepared for comparison using the same preparation method as Bi/Ce. The prepared AP catalysts are shown in Fig. S1a. The Bi/ $Ce_{0.43}$  coat on glass beads (5 mm in diameter, Marienfeld) (designated as G-Bi/ $Ce_{0.43}$ ) was used for the CFEs [12,13]. Briefly, 3 g of Bi/ $Ce_{0.43}$  and 100 g of glass beads were dispersed in 200 mL of distilled water and sonicated for 15 min. The glass beads were separated and dried overnight in an oven at  $60^\circ\text{C}$  followed by calcination at  $500^\circ\text{C}$  for 1 h in air.

### 2.3. Material characterization

The crystal structures of the prepared AP catalysts were analyzed using an X-ray diffractometer (X'Pert Pro, PANalytical, KBSI) with  $Cu K\alpha$  radiation at 40 kV and 40 mA and a step size of  $0.02^\circ$  from  $10^\circ$  to  $100^\circ$ . The morphologies of the AP catalysts were observed by field emission scanning electron microscopy (FESEM, JEOL, JSM-7001 F) equipped with energy dispersive X-ray (EDX) analysis. TEM and HRTEM images were obtained using a Tecnai C2 S-Twin microscope and a Tecnai S2 F30ST microscope in KBSI, respectively. Surface element analysis of the AP catalysts was performed using X-ray photoelectron spectroscopy (XPS, Thermo Fisher Scientific, Al K-alpha system, KBSI) with a passing energy of 200 eV. Fourier-transform infrared spectroscopy (FTIR) spectra of the AP catalysts were recorded using a solid spectrophotometer (JASCO, FTIR-4600) within the scan range of  $650\text{--}4000 \text{ cm}^{-1}$ . The UV-Vis diffuse reflection spectra (DRS) of the plasma catalyst were obtained using a UV-VIS spectrophotometer (Shimadzu UV-VIS) to investigate the light absorption behavior within the range of 200–800 nm. The zero-point charge ( $pH_{ZPC}$ ) of the AP catalysts was investigated using the salt method (detailed information is provided in the Supplementary material, SI). The degree of defects in the AP catalysts was analyzed using electron paramagnetic resonance (EPR, Bruker A200, EMX series). Photoluminescence (PL) and time-resolved PL (TRPL) analyses were conducted using an F-7000 FL Spectrophotometer (Hitachi). The Raman spectra of the AP catalysts were analyzed using a confocal Raman microscope (Alpha 300 R, WiTeC) with a 633 nm Ne-He laser. Metal leaching from AP catalysts was determined by inductively coupled plasma optical emission spectroscopy (ICP-OES). X-ray absorption spectroscopy (XAS) was performed in transmission mode at the 10 C Pohang beamline (ring current of 250 mA at 3.0 GeV) at the Pohang Accelerator Laboratory (PAL, South Korea). The photocurrents and electrochemical impedance spectroscopy (EIS) of the AP catalysts were measured using a potentiostat (Ivium Compact Stat, Eindhoven, Netherlands) fitted with a standard three-electrode system including a Pt rod, Ag/AgCl electrode, and indium tin oxide glass (ITO, surface resistance connected  $\leq 200 \Omega$ ) as the counter, reference, and working electrodes (details presented in SI). The details of the density functional theory (DFT) computational studies are provided in the SI.

## 2.4. Plasma diagnostics

Ar gas (99.999%) was used as the working gas and flowed into a high-voltage stainless-steel electrode located inside a quartz tube (2-mm I.D., 4-mm O.D.) at a flow rate of 2 L/min controlled by a mass flow-meter (Dwyer Instruments, USA). The AP was operated by a high-voltage alternating current (AC) power system with a maximum peak voltage of 13 kV and a 20 Hz sinusoidal wave (Fig. S2). A stainless-steel syringe needle was used as the high-voltage electrode. A metal wire was used as a grounded electrode and wrapped in the outer tube 10 mm below the high-voltage electrode. Finally, Ar gas was discharged between the high-voltage and grounded electrodes and propagated toward the end of the tube. Optical emission spectra (OES, 200–1100 nm) of the AP were recorded using a spectrometer (HR4000CG-UV-NIR, Ocean Optics) equipped with an optical fiber. The OES results showed strong emission of excited N<sub>2</sub> (308–406 nm) and Ar species (696–963 nm) in the AP [14]. The applied voltage and discharge current of the AP were recorded using an oscilloscope (Keysight, DSOX3104T) equipped with a current probe (Tektronix, P6021A) and high-voltage probe (Tektronix, P6015A). The power dissipated by the AP discharge was calculated using the measured voltage and current curves.

## 2.5. PFOA destruction experiments

Batch experiments on AP catalysis for PFOA destruction were carried out in an AP jet catalytic reactor at room temperature (Fig. S1b–c). The details of the plasma diagnostics are provided in the SI. The I–V curve for AP is shown in Fig. S2 and the power dissipations (22.8–24.6 W) of AP using different water matrices indicated insignificant differences in the dissipated power, indicating the stability of AP (Fig. S4). Fig. S3 shows the OES of the AP; the emitted light ranged from 300 to 1000 nm, indicating the UV to VIS range. To prevent the leaching of Per- and polyfluoroalkyl substances (PFAS), the fabricated AP jet did not contain any Teflon products. In addition, we analyzed the PFAS concentration of AP jet-treated distilled water using a liquid chromatography system with a triple quadrupole mass spectrometer (LC-MS-MS) to ensure that the PFAS was not leached from the AP catalysis. In a typical plasma catalysis run, 5 mg of the catalyst was added to 25 mL of PFOA solution (20 mg L<sup>-1</sup>). The suspension was stirred at 200 rpm at room temperature. Meanwhile, 1 mL of water sample was collected at intervals from min 2–30 and filtered using a 0.45 µm-pore syringe filter. The filtrates were analyzed using high-performance liquid chromatography (Agilent 1200 infinity series) fitted with a C18 column (details in SI). The electrical energy per order (E<sub>EO</sub>) for PFOA removal and the 50% PFOA degradation per kWh energy consumption (G<sub>50</sub>) were calculated to investigate the energy requirement using the AP or AP catalyst (details in SI). Scavenger experiments were conducted to investigate the main reactive species in PFOA destruction. Tert-butyl alcohol (10 mM), sodium sulfate (10 mM), sodium oxalate (10 mM), and 1,4-benzoquinone (10 mM) were used to capture ·OH, e<sup>-</sup>, h<sup>+</sup>, and ·O<sub>2</sub><sup>-</sup>, respectively. To investigate the practicability of the AP catalyst, PFOA removal experiments were conducted using PFOA-spiked wastewater effluent (Seoul, South Korea), and the water matrix is shown in Table S1. Furthermore, we conducted experiments using low-level PFOA (180–400 ng L<sup>-1</sup>) containing synthetic water to investigate the actual application of the proposed AP catalysis. LC-MS-MS (TSQ ALTIS, Thermo Fisher Scientific, Germany) was used to measure the remaining sub-ng L<sup>-1</sup> concentration of PFOA and to investigate the intermediate species (by-products) during kinetics (Tables S2 and S3). The amounts of fluoride ions (F<sup>-</sup>) released from the reaction were analyzed using a fluoride meter (Mettler Toledo). All experiments were conducted in duplicate. Hydrogen peroxide (H<sub>2</sub>O<sub>2</sub>) and ozone (O<sub>3</sub>) concentrations were quantified using iodometric [15] and indigo methods [16], respectively (details in the SI).

## 2.6. Continuous flow experiments

CFEs were conducted to investigate the applicability of AP catalysis for PFOA removal using 50 g G-Bi/Ce<sub>0.43</sub>. The reactor for the CFEs was custom-made with Pyrex glass (working volume: 250 mL; total volume: 300 mL) (Fig. S5). The CFEs for PFOA removal were conducted using three AP jets, and the inlet flow rate was controlled using a peristaltic pump. The effluents of the CFEs were collected and the remaining PFOA concentrations were analyzed using LC-MS-MS.

## 3. Results and discussion

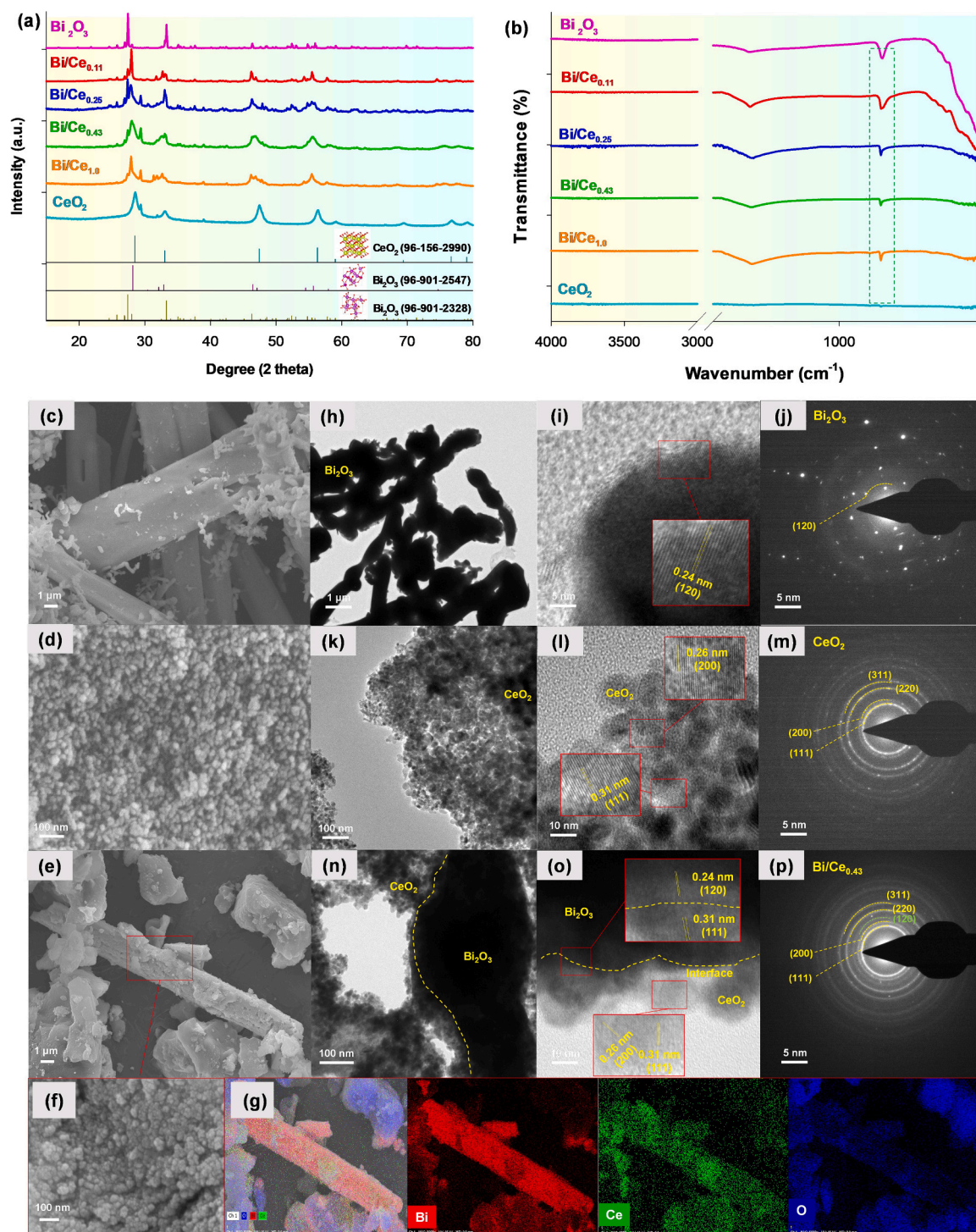
### 3.1. Material characterization

Fig. 1a shows the XRD patterns of CeO<sub>2</sub> and its composite catalysts, where the peaks correspond to cubic CeO<sub>2</sub> with *Fm3m* space group (JCPDS, 34–0394). In addition, Bi<sub>2</sub>O<sub>3</sub> had a monoclinic structure (α-Bi<sub>2</sub>O<sub>3</sub>, JCPDS:96–901–2547). Based on the R<sub>wp</sub>, R<sub>p</sub>, and χ<sup>2</sup> tests, the experimental XRD patterns were consistent with the Rietveld refinement calculations (Table S4). Owing to the atomic reorganization of Ce, the increment of Ce doping in Bi<sub>2</sub>O<sub>3</sub> resulted in a decrease in the CeO<sub>2</sub> unit cell parameter [17]. In addition, the increase in Ce doping ratio led to the formation of the tetragonal phase Bi<sub>2</sub>O<sub>3</sub> (β-Bi<sub>2</sub>O<sub>3</sub>). The XRD results showed that Bi<sub>2</sub>O<sub>3</sub>, CeO<sub>2</sub>, and composites of Bi<sub>2</sub>O<sub>3</sub> and CeO<sub>2</sub> (Bi/Ce composite) were successfully prepared via facile precipitation followed by calcination. Fig. 1b shows the FTIR spectra, exhibiting a stretching vibration at 800 cm<sup>-1</sup> for the Bi<sub>2</sub>O<sub>3</sub> phase in the prepared catalysts. As the Ce doping ratio increased, the intensity of the Bi<sub>2</sub>O<sub>3</sub> peaks decreased.

Based on FESEM and HRTEM analyses, Bi<sub>2</sub>O<sub>3</sub> exhibited a rod-type structure (Fig. 1c, h), while pure CeO<sub>2</sub> exhibited a spherical structure (Fig. 1g). Bi/Ce<sub>0.43</sub> (Fig. 1e–f) showed that the CeO<sub>2</sub> nanospheres (average particle size of 10 nm) were doped on the Bi<sub>2</sub>O<sub>3</sub> rod. In addition, the elemental mapping of Ce, O, and Bi for Bi/Ce<sub>0.43</sub> indicated that Ce was homogeneously doped on the Bi<sub>2</sub>O<sub>3</sub> rod (Fig. 1g). Notably, Bi/Ce<sub>0.11</sub>, Bi/Ce<sub>0.25</sub>, and Bi/Ce<sub>1.0</sub> showed similar morphologies in the FESEM analysis (Fig. S6). The single crystallite lattice (1 2 0) (Fig. 1i) detected on the rod and the (1 2 0) Miller index in the SAED analysis (Fig. 1j) corresponded to single-crystalline α-Bi<sub>2</sub>O<sub>3</sub> [18]. Further, HRTEM analysis showed the nanosphere structure of CeO<sub>2</sub> (Fig. 1k) with lattice (1 1 1) and (2 0 0) (Fig. 1l). In addition, the SAED pattern shows the (1 1 1), (2 0 0), (2 2 0), and (3 3 1) Miller indices, referring to CeO<sub>2</sub> (Fig. 1m). The HRTEM imaging showed that Bi/Ce<sub>0.43</sub> exhibited spherical CeO<sub>2</sub> doped on Bi<sub>2</sub>O<sub>3</sub> nanorods (Fig. 1n). The CeO<sub>2</sub> lattices (1 1 1) had interfacial contact with the (1 2 0) phases of Bi<sub>2</sub>O<sub>3</sub> on the Bi/Ce<sub>0.43</sub> composite (Fig. 1o). In addition, the SAED ring showed that the polycrystalline structure was consistent with the crystalline structures of Bi<sub>2</sub>O<sub>3</sub> and CeO<sub>2</sub> in Bi/Ce<sub>0.43</sub> (Fig. 1p).

UV–VIS DRS analysis was conducted to investigate the light absorption properties and bandgap (E<sub>g</sub>) of prepared catalysts (Fig. 2a). Consequently, the Bi/Ce composites exhibited higher absorbance tails in the visible range. Based on the Tauc plots, the E<sub>g</sub> of Bi<sub>2</sub>O<sub>3</sub>, Bi/Ce<sub>0.11</sub>, Bi/Ce<sub>0.25</sub>, Bi/Ce<sub>0.43</sub>, Bi/Ce<sub>1.0</sub>, and CeO<sub>2</sub> were calculated to be 2.68, 2.0, 1.95, 1.89, 1.92, and 2.88 eV, respectively (Fig. S7). Therefore, the Bi/Ce composites had a lower E<sub>g</sub> than pristine materials. In other words, the addition of Ce to Bi<sub>2</sub>O<sub>3</sub> significantly reduces the overall E<sub>g</sub> (Fig. S8a). The light absorbance profile and E<sub>g</sub> of the Bi/Ce composites suggest that the composites could be activated by UV–VIS light emitted from the AP, as observed by OES analysis (300–420 and 700–950 nm) (Fig. S3). Meanwhile, Bi/Ce<sub>0.43</sub> had the highest photocurrent density, followed by Bi/Ce<sub>1.0</sub>, Bi/Ce<sub>0.11</sub>, Bi/Ce<sub>0.25</sub>, CeO<sub>2</sub>, and Bi<sub>2</sub>O<sub>3</sub> (Fig. 2b), indicating that Bi/Ce<sub>0.43</sub> could produce the highest e<sub>aq</sub><sup>-</sup> under UVA. EIS analysis showed that the Bi/Ce composites exhibited a smaller arc radius than pristine CeO<sub>2</sub> or Bi<sub>2</sub>O<sub>3</sub> (Fig. 2c). This result indicates that the Bi/Ce composites have lower internal charge transfer resistance and higher electronic conductivity [19]. In particular, Bi/Ce<sub>0.43</sub> exhibits the smallest arc radius. Therefore, Bi/Ce<sub>0.43</sub> had the highest internal charge transfer





**Fig. 1.** XRD (a) and FTIR (b) analysis for  $\text{Bi}_2\text{O}_3$ ,  $\text{Bi/Ce}_{0.11}$ ,  $\text{Bi/Ce}_{0.25}$ ,  $\text{Bi/Ce}_{0.43}$ ,  $\text{Bi/Ce}_{1.0}$  and  $\text{CeO}_2$ . FESEM imaging for  $\text{Bi}_2\text{O}_3$  (c),  $\text{CeO}_2$  (d),  $\text{Bi/Ce}_{0.43}$  (e) and zoom in  $\text{Bi/Ce}_{0.43}$  (f). FESEM-EDX mapping for  $\text{Bi/Ce}_{0.43}$  (g). HRTEM imaging and SAED analysis for  $\text{Bi}_2\text{O}_3$  (h-j),  $\text{CeO}_2$  (k-m), and  $\text{Bi/Ce}_{0.43}$  (n-p).

performance among the Bi/Ce composites and produced the highest number of charge carriers in AP catalysis.

Furthermore, M-S analysis showed that the prepared catalysts had positive slopes as n-type semiconductors, where the Fermi level positions were located near the conduction band (CB) (Fig. 2d) [20]. Accordingly, the flat band potentials ( $E_{fb}$ ) of  $\text{Bi}_2\text{O}_3$ ,  $\text{Bi/Ce}_{0.11}$ ,  $\text{Bi/Ce}_{0.25}$ ,  $\text{Bi/Ce}_{0.43}$ ,  $\text{Bi/Ce}_{1.0}$ , and  $\text{CeO}_2$  were calculated to be  $-1.096$ ,  $-0.982$ ,  $-0.986$ ,  $-0.996$ ,  $-0.969$ , and  $-0.998$  V vs. NHE, respectively. Therefore,  $\text{CeO}_2$  doping on  $\text{Bi}_2\text{O}_3$  reduced  $E_{fb}$ . Generally, the CB minimum (CBM) for n-type semiconductors is 0.1 V higher than  $E_{fb}$  [21]. The

proposed band structures of the Bi/Ce composite, obtained by combining the results of the M-S plot and Tauc plot analyses, are presented in Fig. S8b. The donor densities were also obtained via M-S analysis (Table S8), indicating that an increase in the Ce doping ratio increased the donor density. In summary, the Bi/Ce composite exhibited more optimized charge-transfer properties than pristine  $\text{CeO}_2$  or  $\text{Bi}_2\text{O}_3$  for AP catalysis.



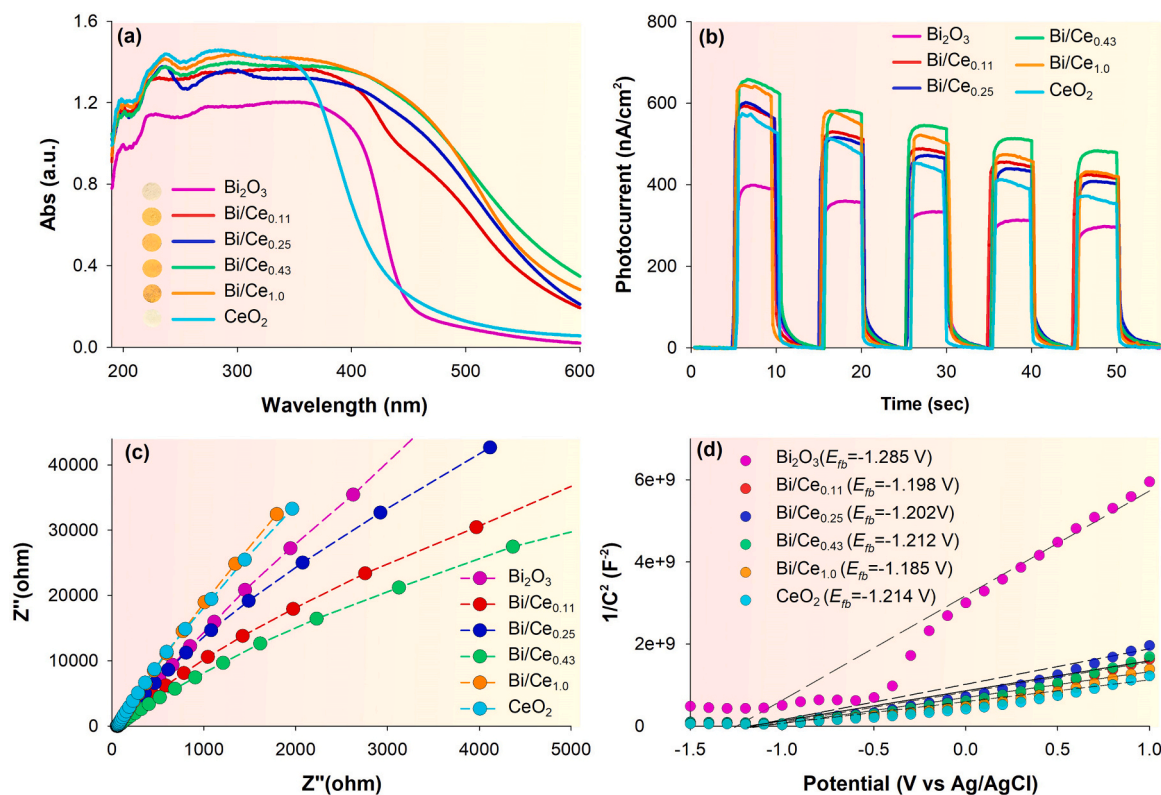


**Fig. 2.** UV-VIS DRS (Insert figure showed the image of prepared catalysts) (a), Photocurrent density (b), EIS (c), and M-S plot (d) for Bi<sub>2</sub>O<sub>3</sub>, Bi/Ce<sub>0.11</sub>, Bi/Ce<sub>0.25</sub>, Bi/Ce<sub>0.43</sub>, Bi/Ce<sub>1.0</sub> and CeO<sub>2</sub>.

### 3.2. PFOA destruction performance

Fig. 3a shows the kinetics of PFOA removal under AP catalysis using the prepared catalysts. All kinetic rate constants for PFOA removal are presented in Table S5 and the defluorination percentages of PFOA are in Table S6. The kinetic rate constants ( $k$ ) for AP, AP-Bi<sub>2</sub>O<sub>3</sub>, AP-Bi/Ce<sub>0.11</sub>, AP-Bi/Ce<sub>0.25</sub>, AP-Bi/Ce<sub>0.43</sub>, AP-Bi/Ce<sub>1.0</sub>, and AP-CeO<sub>2</sub> were 0.026, 0.029, 0.043, 0.097, 0.149, 0.041, and 0.022 min<sup>-1</sup>, respectively (Fig. 3b). Along with the PFOA removal kinetics, the AP-Bi/Ce<sub>0.43</sub> (16.1%) exhibited the highest defluorination performance at 30 min, followed by AP-Bi/Ce<sub>0.25</sub> (11.4%), AP-Bi/Ce<sub>0.11</sub> (10.9%), AP-Bi<sub>2</sub>O<sub>3</sub> (9.9%), AP-Bi/Ce<sub>1.0</sub> (7.3%), AP (6.3%) and AP-CeO<sub>2</sub> (4.9%) (Fig. S9). Accordingly, the addition of the Bi/Ce composite to the AP system improved the PFOA removal kinetic rate and defluorination percentage. The leached concentrations of Ce(III) and Bi(III) from AP-Bi/Ce<sub>0.43</sub> were not detected [detection limits: 50  $\mu\text{g L}^{-1}$  for Ce(III) and 100  $\mu\text{g L}^{-1}$  for Bi(III)] by ICP-OES. This result indicates the high stability of the prepared catalysts (Table S7). In addition, to investigate the synergistic effect of PFOA destruction by AP catalysis, PFOA adsorption tests using the prepared catalysts were conducted as control experiments (absence of AP). As a result, the PFOA removal percentage of Bi<sub>2</sub>O<sub>3</sub> was less than 20% (Fig. S10). The increase in Ce doping ratio slightly enhanced the PFOA sorption, while pure CeO<sub>2</sub> yielded a removal percentage of approximately 45% at 30 min (Fig. S8a). This result is attributed to the increase in the pH of the zero-point charge (pH<sub>ZPC</sub>) as the Ce doping ratio increased (Fig. S11). As pH<sub>ZPC</sub> increased, the catalysts exhibited a more positive charge, which could be more favorable for negatively charged PFOA (pK<sub>a</sub> ~ 2.5) adsorption [22]. Although CeO<sub>2</sub> exhibited the highest PFOA removal adsorption performance, there was no significant enhancement in PFOA removal when combined with AP. Moreover, the equation (eq. S4) in the SI was used to calculate the synergistic factor (SF). The SF values were calculated to be 0.78, 1.19, 2.67, 4.2, 1.06, and 0.53 for Bi<sub>2</sub>O<sub>3</sub>, Bi/Ce<sub>0.11</sub>, Bi/Ce<sub>0.25</sub>, Bi/Ce<sub>0.43</sub>, Bi/Ce<sub>1.0</sub>, and CeO<sub>2</sub>, respectively. Therefore, the Bi/Ce composite exhibited a high SF (> 1)

for PFOA removal, while no enhancement was observed with pristine Bi<sub>2</sub>O<sub>3</sub> and CeO<sub>2</sub>. An increase in the Ce doping ratio increased to SF; however, a Ce doping ratio beyond 30% exhibited a deterioration of the synergistic effect. To elucidate the high SF of the Bi/Ce composite, H<sub>2</sub>O<sub>2</sub> and O<sub>3</sub> measurements were conducted (Fig. 3c–d). Under AP alone, O<sub>3</sub> linearly increased to 5.8 mg L<sup>-1</sup> for 30 min, while H<sub>2</sub>O<sub>2</sub> rapidly increased for 5 min, followed by a steady increase to 23 mg L<sup>-1</sup>. In particular, lower O<sub>3</sub> and H<sub>2</sub>O<sub>2</sub> concentrations were detected as the Ce doping ratio in the Bi/Ce composite increased. This result is attributed to the CeO<sub>2</sub> redox properties that could catalytically decompose O<sub>3</sub> and H<sub>2</sub>O<sub>2</sub> produced from AP into  $\cdot\text{OH}$  [23]. Therefore, additional experiments were conducted to determine the mechanism of PFOA destruction using AP catalysis.

A wide scan of XPS analysis was conducted to investigate the elemental composition of the catalysts (Fig. S12). The O1s spectrum was deconvoluted into four peaks at ~529, 530, 532, and 535 eV corresponding to lattice oxygen (O<sub>L</sub>), O<sub>V</sub>, adsorbed oxygen (O<sub>abs</sub>), and adsorbed electrically isolated OH or H<sub>2</sub>O (O<sub>e-abs</sub>), respectively (Fig. 4a) [24]. The details of the peak positions for XPS analysis are presented in Table S9. Bi<sub>2</sub>O<sub>3</sub>, Bi/Ce<sub>0.11</sub>, Bi/Ce<sub>0.25</sub>, Bi/Ce<sub>0.43</sub>, Bi/Ce<sub>1.0</sub>, and CeO<sub>2</sub> yielded 35.2%, 26.5%, 30.1%, 40.7%, 26%, and 33.4% of O<sub>V</sub> percentage, respectively. Except for Bi/Ce<sub>1.0</sub>, the increase in Ce doping ratio promoted O<sub>V</sub> formation. In addition, compared to pristine Bi<sub>2</sub>O<sub>3</sub>, the Ce doping of Bi<sub>2</sub>O<sub>3</sub> caused the O<sub>L</sub> peak to shift to lower binding energy and the O<sub>V</sub> peak to higher binding energy, indicating that electron density increases in O<sub>L</sub> and decreases in O<sub>V</sub>. This may be attributed to the chemical composition of CeO<sub>2</sub> in Bi<sub>2</sub>O<sub>3</sub> [25]. In addition, EPR solid analysis showed that Bi<sub>2</sub>O<sub>3</sub> exhibited a g-value of 2.008, which corresponds to the unpaired electrons (Fig. S13a) [26]. The increase in Ce doping ratio reduced the spin line intensity and shifted the lower g-value owing to the increase in the average distance between metals and oxygen sites, resulting in differences in orbital contribution and spin-spin coupling. The Ce3d spectra were deconvoluted into 8 peaks corresponding to Ce(III) and Ce(IV) [21] (Fig. 4b), and the deconvoluted data

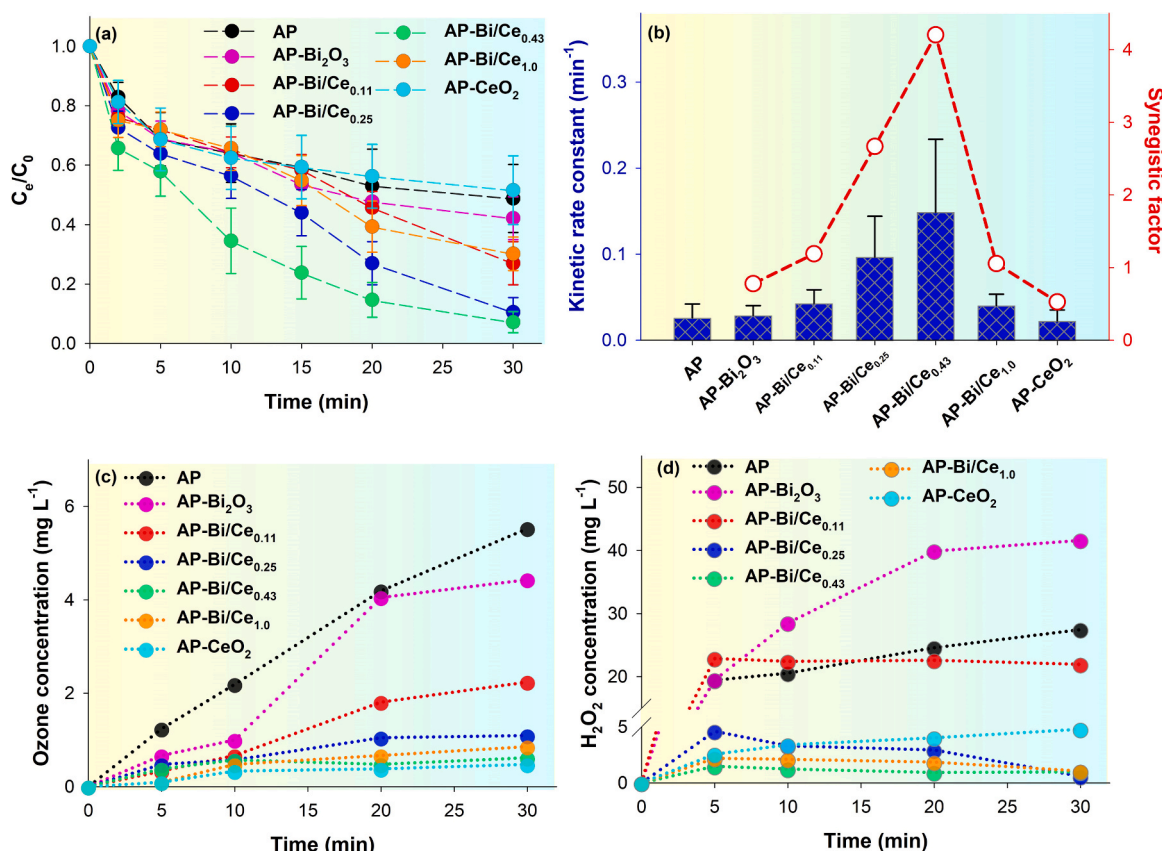


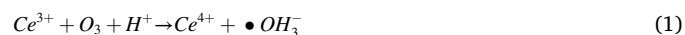
**Fig. 3.** PFOA kinetic removal using AP, AP-Bi<sub>2</sub>O<sub>3</sub>, AP-Bi/Ce<sub>0.11</sub>, AP-Bi/Ce<sub>0.25</sub>, AP-Bi/Ce<sub>0.43</sub>, AP-Bi/Ce<sub>1.0</sub> and AP-CeO<sub>2</sub> (a) and kinetic rate constants for PFOA removal experiments (b). Ozone (c) and hydrogen peroxide (d) concentration measurement for AP and AP/catalyst system. Experiment configuration: Argon gas flow rate: 2LPM, PFOA initial concentration: 20 mg L<sup>-1</sup>, catalyst mass: 5 mg, solution volume: 25 mL).

for Ce3d were presented in Table S9. Notably, Bi/Ce<sub>0.43</sub> exhibited a higher Ce(III) (25.9%) and O<sub>V</sub> percentages (40.7%) compared to pristine CeO<sub>2</sub> (Ce(III): 25.0%, O<sub>V</sub>: 33.4%). The Bi4f spectra for AP catalysts revealed that Bi peak intensity decreased and doublet peaks shifted to lower binding energy as the Ce doping ratio increased (Fig. 4c). This result indicated the chemical bond formation between CeO<sub>2</sub> and Bi<sub>2</sub>O<sub>3</sub> in Bi/Ce composite [27]. Notably, O<sub>V</sub> percentages and PFOA removal kinetic constants using AP catalysis were found to be strongly linearly correlated (R<sup>2</sup>, 0.946) (Fig. 4d). However, the Ce(III) percentages had an insignificant linear relationship with PFOA removal kinetic constants (Fig. S13b). Therefore, the O<sub>V</sub> presence plays a significant role in PFOA destruction by AP catalysis, and Bi/Ce<sub>0.43</sub> was found to be the optimal catalyst for PFOA removal.

### 3.3. PFOA removal mechanism

To investigate the effect of the reactive species on PFOA removal, quenching experiments for AP or AP-Bi/Ce<sub>0.43</sub> were conducted (Fig. 5). Scavenger experiment results revealed that e<sub>aq</sub><sup>-</sup> and ·OH scavengers significantly suppressed the PFOA removal for both AP (Fig. 5a) and AP-Bi/Ce<sub>0.43</sub> (Fig. 5b). The PFOA removal kinetic rate constants in the absence (control) and presence of e<sub>aq</sub><sup>-</sup>, ·OH, h<sup>+</sup>, and ·O<sub>2</sub><sup>-</sup> scavengers were 0.026, 0.005, 0.011, 0.024, and 0.021 min<sup>-1</sup> for AP, and 0.148, 0.004, 0.009, 0.076, and 0.045 min<sup>-1</sup> for AP-Bi/Ce<sub>0.43</sub> (Fig. 5c), respectively. Interestingly, the presence of e<sub>aq</sub><sup>-</sup> scavenger shows 87% and 97% quenching effect on PFOA destruction in AP and AP-Bi/Ce<sub>0.43</sub>, respectively. In contrast, the h<sup>+</sup> scavenger was negligible for PFOA destruction in both systems. ESR spin trap analyses were performed to investigate the ROS generation in AP and AP-Bi/Ce<sub>0.43</sub>. Fig. 5d shows the signal production of H<sub>2</sub>O<sub>2</sub>, O<sub>3</sub>, and ·O<sub>2</sub><sup>-</sup> in AP and AP-Bi/Ce<sub>0.43</sub>. Compared to

sole AP, AP-Bi/Ce<sub>0.43</sub> exhibited lower ESR spin trap signals, suggesting lower O<sub>3</sub>, H<sub>2</sub>O<sub>2</sub>, and ·O<sub>2</sub><sup>-</sup> production at 1 and 3 min. This result was consistent with the lower O<sub>3</sub> and H<sub>2</sub>O<sub>2</sub> concentrations in AP-Bi/Ce<sub>0.43</sub>, shown in Figs. 3c and 3d. Meanwhile, AP-Bi/Ce<sub>0.43</sub> exhibited a higher TEMP-<sup>1</sup>O<sub>2</sub> signal than sole AP (Fig. 5e). This result revealed that Bi/Ce<sub>0.43</sub> addition to AP enhances the <sup>1</sup>O<sub>2</sub> formation. Zhang, Xiong, Wei, Song, Ren, Xu and Lai [28] reported that <sup>1</sup>O<sub>2</sub> production in the catalytic ozonation occurs mainly from the reaction of water molecules with ·O<sub>2</sub><sup>-</sup>. Therefore, the lower ·O<sub>2</sub><sup>-</sup> peak signals detected in AP-Bi/Ce<sub>0.43</sub> might correlate to higher <sup>1</sup>O<sub>2</sub> formation. Moreover, as the peak intensity of 1:2:2:1 signals for AP-Bi/Ce<sub>0.43</sub> increased up to 2.2 times for 3 min, the Bi/Ce<sub>0.43</sub> addition into AP resulted in higher ·OH formation (Fig. 5f and g). Based on Eqs. (1) and (2), the CeO<sub>2</sub> properties could improve O<sub>3</sub> decomposition into ·OH via the facilitation of redox Ce(III)/Ce(IV) [23, 29]:



The results of the scavenger tests concluded that e<sub>aq</sub><sup>-</sup> and ·OH were the major reactive species, contributing to PFOA destruction by AP-Bi/Ce<sub>0.43</sub>. Additionally, we obtained DMPO-H electron adduct signals (Fig. 5h). Surprisingly, Bi/Ce<sub>0.43</sub> addition into AP induced 5.2 times higher e<sub>aq</sub><sup>-</sup> than AP alone [30]. Therefore, to investigate the effect of UV light emitted from AP on PFOA destruction by AP-Bi/Ce<sub>0.43</sub>, additional experiments were conducted by supplying only ionized gas from AP to Bi/Ce<sub>0.43</sub> (Fig. S14). Therefore, the kinetic rate constant for PFOA destruction using AP (0.026 min<sup>-1</sup>) was retarded by 38.7% with UV-cut off (0.016 min<sup>-1</sup>). AP-Bi/Ce<sub>0.43</sub> (UV-cut off) had an approximately 65% lower kinetic rate constant (0.052 min<sup>-1</sup>) than AP-Bi/Ce<sub>0.43</sub>

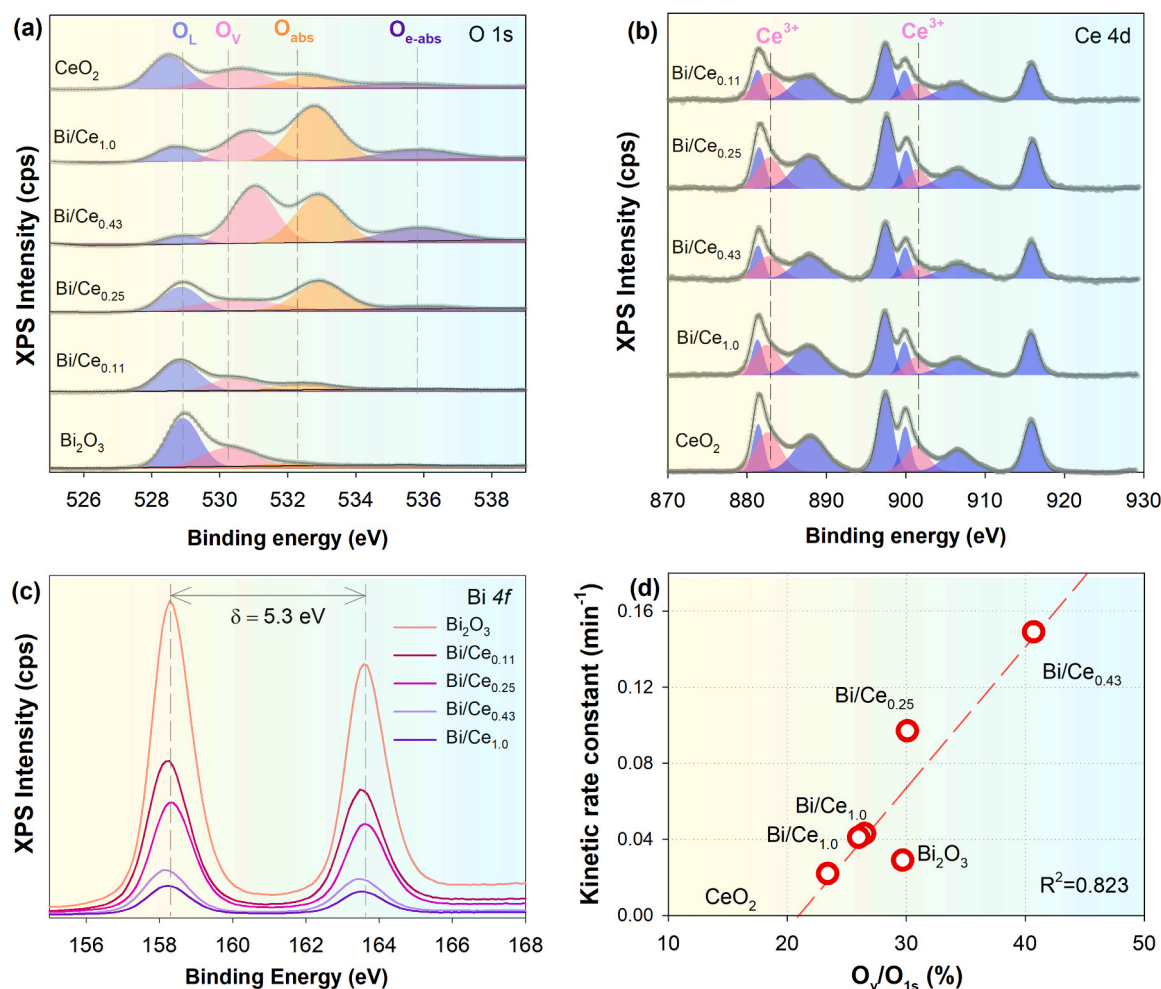


**Fig. 4.** XPS analysis of O1s (a), Ce4d (b),  $\text{Ce}^{3+}$  corresponding to pink filled area and  $\text{Ce}^{4+}$  corresponded to purple filled area, Bi4f (c) for  $\text{Bi}_2\text{O}_3$ ,  $\text{Bi/Ce}_{0.11}$ ,  $\text{Bi/Ce}_{0.25}$ ,  $\text{Bi/Ce}_{0.43}$ ,  $\text{Bi/Ce}_{0.10}$  and  $\text{CeO}_2$  and correlation between  $\text{O}_V$  and PFOA removal (d).

( $0.149 \text{ min}^{-1}$ ). Overall, AP- $\text{Bi/Ce}_{0.43}$  was 3.3 and 5.7 fold faster than sole AP in the absence and presence of UV, respectively. Therefore, the UV emission from AP could have a significant synergistic effect on  $\text{Bi/Ce}_{0.43}$  for PFOA destruction.

Photoluminescence and time-resolved photoluminescence analyses were performed to investigate the behavior of charge-carrier recombination of AP catalysts. The PL spectra revealed that the  $\text{Bi/Ce}_{0.43}$  has lower peak intensity than pristine  $\text{Bi}_2\text{O}_3$  and  $\text{CeO}_2$ , displaying a higher carrier spatial separation efficiency (Fig. 6a). In addition,  $\text{Bi/Ce}_{0.43}$  had a PL peak shifted to a higher wavelength. Therefore,  $\text{Bi/Ce}_{0.43}$  requires lower excitation energy than pristine  $\text{Bi}_2\text{O}_3$  and  $\text{CeO}_2$ . This is consistent with the UV-VIS DRS analysis result, where  $\text{Bi/Ce}_{0.43}$  has a relatively smaller  $E_g$  than  $\text{Bi}_2\text{O}_3$  or  $\text{CeO}_2$ . The average electron decay times obtained from the TRPL analysis for  $\text{Bi}_2\text{O}_3$ ,  $\text{CeO}_2$ , and  $\text{Bi/Ce}_{0.43}$  were 0.363, 5.85, and 2.59 ns (Fig. 6b), respectively. Therefore,  $\text{CeO}_2$  doping on  $\text{Bi}_2\text{O}_3$  increased the carrier lifetime of sole  $\text{Bi}_2\text{O}_3$  (Table S10). The TRPL mapping images show that  $\text{Bi}_2\text{O}_3$  has a strong blue luminescence intensity associated with a shorter electron lifetime than  $\text{CeO}_2$  (Fig. 6c). Overall, the PL and TRPL results implied that  $\text{CeO}_2$  doping on  $\text{Bi}_2\text{O}_3$  could modulate the charge transfer by providing a non-radiative pathway via ample heterojunction interfaces for separating  $e^-/h^+$  pairs and suppressing the charge recombination [31]. Significantly, the charge recombination reduction could enhance the  $e^-_{aq}$  production in the aqueous phase, leading to increased PFOA destruction by AP catalysis.

Raman analysis showed that  $\text{Bi}_2\text{O}_3$  exhibited peaks at 126, 152, 199, 273, 323, and  $533 \text{ cm}^{-1}$  (Fig. 6d) [32]. Furthermore,  $\text{CeO}_2$  presented a

peak at  $461 \text{ cm}^{-1}$ , corresponding to the  $F2g$  mode of cubic fluorite structure metal dioxide. The Raman vibration at  $1063 \text{ cm}^{-1}$  in  $\text{CeO}_2$  corresponds to the second-order phonon mode, and its shift to a higher wavelength ( $1064 \text{ cm}^{-1}$ ) in  $\text{Bi/Ce}_{0.43}$  represents defect formation in the  $\text{CeO}_2$  lattice [33]. After compositing with  $\text{CeO}_2$ , the  $\text{Bi}_2\text{O}_3$  peaks shifted from 273 to 274 and  $322\text{--}313 \text{ cm}^{-1}$ , respectively. In addition, the Raman peak shift ( $461\text{--}444 \text{ cm}^{-1}$ ) and the increased peak intensity at  $1064 \text{ cm}^{-1}$  in  $\text{Bi/Ce}_{0.43}$  may be due to  $\text{Ce(III)}$  formation in  $\text{CeO}_2$ . The downshift of the Raman peaks in  $\text{Bi/Ce}_{0.43}$  is mainly attributed to the lattice expansion and mode softening induced by spin-phonon coupling [34]. This phenomenon occurs when  $\text{O}_V$  is created in  $\text{Bi/Ce}_{0.43}$  owing to the  $\text{Ce(IV)}(0.97 \text{ \AA})$  replacement by  $\text{Ce(III)}$ , which has a higher ionic radius ( $1.143 \text{ \AA}$ ) [35].

Further, XAS analysis at the O  $k$ -edge was conducted to investigate the bonding and symmetry properties of the X-ray excited oxygen atom (Fig. 7a and S15–16). Compared to pristine  $\text{CeO}_2$ , the  $\text{Bi/Ce}_{0.43}$  had decreased peak intensities in total fluorescence yield (TFY). This result reflected a reduction in the unoccupied  $4f$  states of Ce owing to the  $\text{O}_V$  formation. The  $\text{O}_V$  existence could reduce the energy of Ce  $d$  and  $f$  orbital, bringing it closer to the Fermi level and lowering the valence of Ce ions [36]. In addition,  $\text{Bi/Ce}_{0.43}$  showed that the reduction of peak and peak positions shifted to high binding energies of O  $k$ -edge in the TFY spectra compared to those of pristine  $\text{CeO}_2$  (Fig. S16), indicating relatively high efficiency of electron transfer in  $\text{Bi/Ce}_{0.43}$ . Meanwhile, the TFY Ce3d spectrum of  $\text{Bi/Ce}_{0.43}$  revealed that the main peaks in the Ce M4,5 edge shifted to lower binding energies than those of pristine



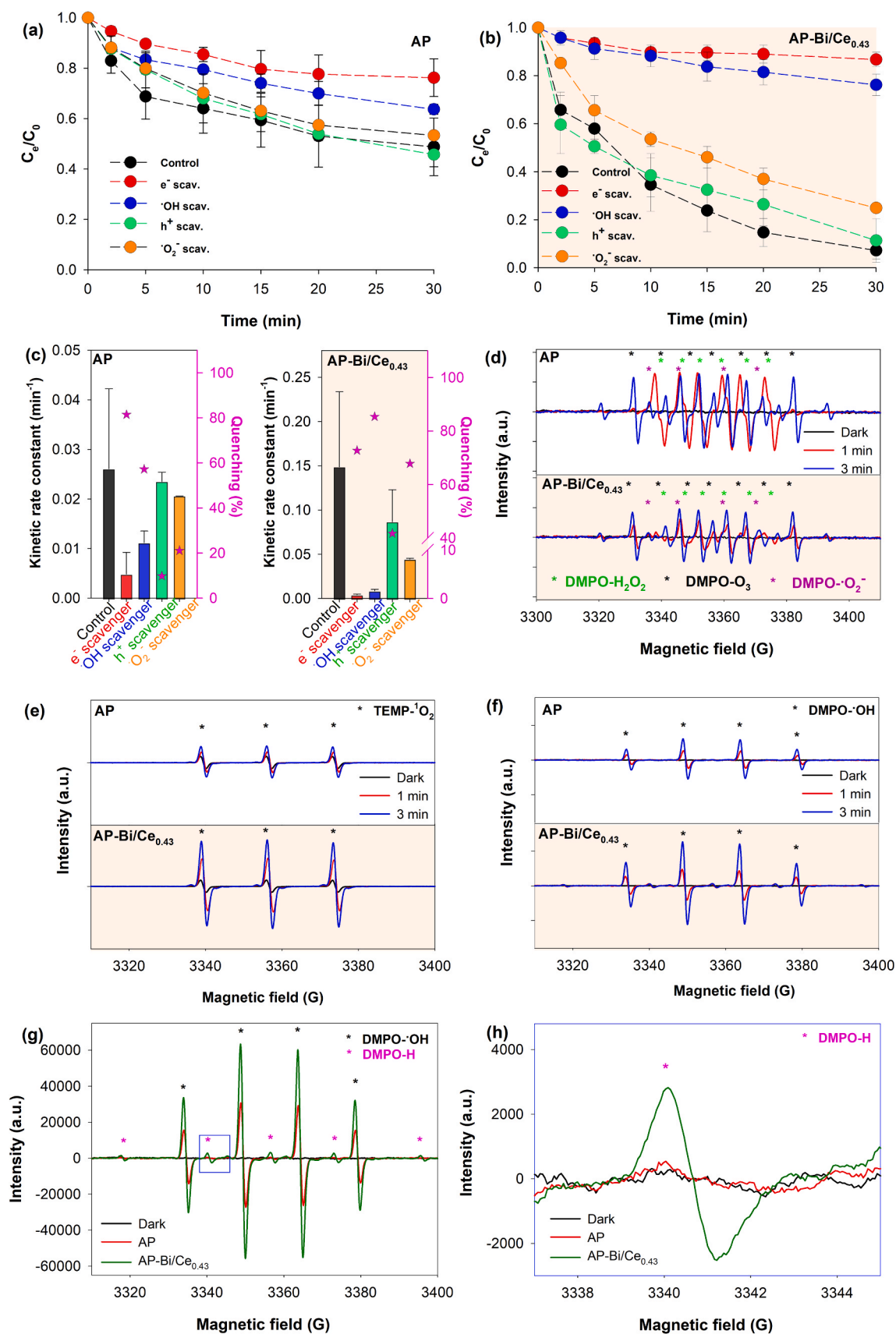


**Fig. 5.** Scavenger experiments for AP (a) and AP-BiCe<sub>0.43</sub> (b). Quenching percentage for scavenger experiments (c). ESR spin trap experiment for AP and AP-BiCe<sub>0.43</sub> in DMPO/methanol(d), TEMP (e) and DMPO/water (f). ESR spin trap experiment for AP and AP-BiCe<sub>0.43</sub> in DMPO/water at 3 min (g) and insert blue box (h).

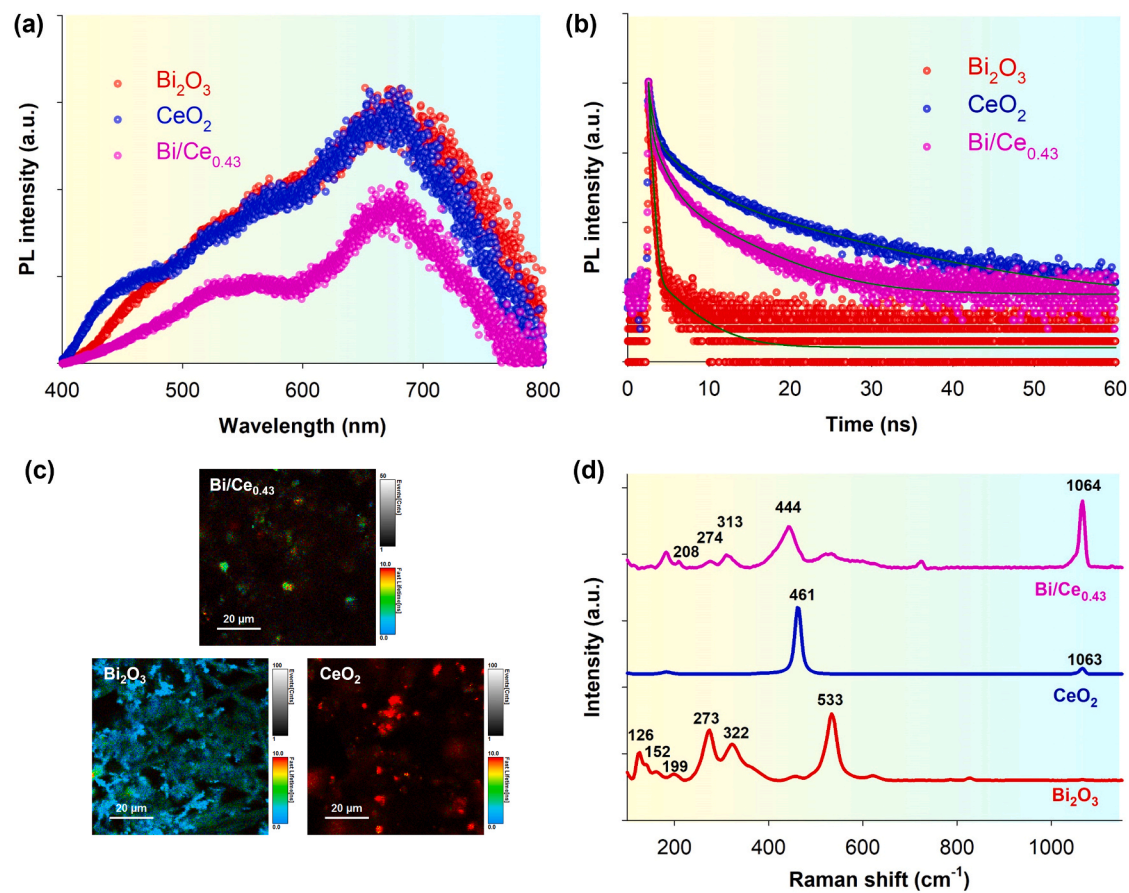
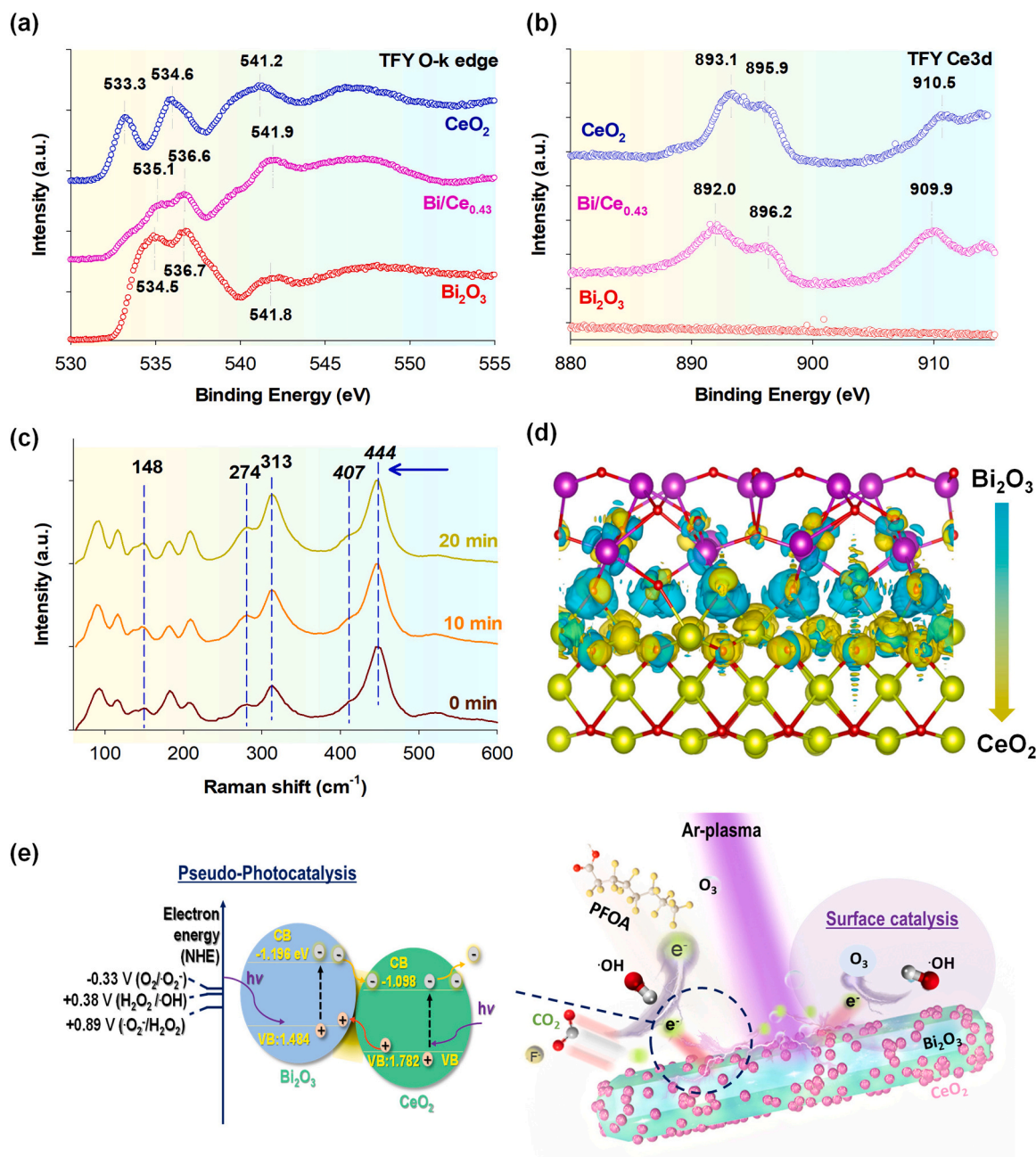


Fig. 6. PL (a), TRPL (b), TRPL mapping (c), Raman (d) analysis for  $\text{Bi}_2\text{O}_3$ ,  $\text{CeO}_2$  and  $\text{Bi/Ce}_{0.43}$ .



**Fig. 7.** XAS (a-b) analysis for Bi<sub>2</sub>O<sub>3</sub>, CeO<sub>2</sub> and Bi/Ce<sub>0.43</sub>. Time-lapse raman analysis for Bi/Ce<sub>0.43</sub> under AP system at time 0, 10 and 20 mins. The charge density difference of Bi/Ce<sub>0.43</sub> heterojunction catalyst calculated by DFT (d). Proposed mechanism of Bi/Ce<sub>0.43</sub> for PFOA destruction under argon jet plasma system (e).

CeO<sub>2</sub>. This result indicated a higher electron density accumulated in the Ce 6*f* in Bi/Ce<sub>0.43</sub> (Fig. 7b) [36,37]. Further, this phenomenon was obtained in all Bi/Ce composites (Fig. S17). Conversely, the total electron yield (TEY) results showed that the Bi/Ce<sub>0.43</sub> exhibited lower binding energies in the Ce M4,5 edge than pristine CeO<sub>2</sub>, representing higher Ce(III) existence (Fig. S18).

Furthermore, Raman time-lapse analysis was performed to investigate the chemical properties of Bi/Ce<sub>0.43</sub> under AP (Fig. 7c). As a result, the down-shift of F2g peak at 444 cm<sup>-1</sup> occurred at 10 and 20 min, indicating Ce(IV) reduction to Ce(III) owing to pseudo-photocatalysis under AP [38]. In addition, the increased peak intensities at 148, 274, 313, and 407 cm<sup>-1</sup> can be attributed to the higher oxygen vibration with Bi as the interaction time in AP increases [39].

According to XPS and XAS analyses, the electron-rich zone on CeO<sub>2</sub> was observed. To further elucidate the electron interaction in Bi/Ce<sub>0.43</sub>,

DFT calculation were conducted. The DFT simulations to investigate the change in the density of states (DOS) in CeO<sub>2</sub>, Bi<sub>2</sub>O<sub>3</sub>, and Bi/Ce<sub>0.43</sub>. DFT simulation revealed that the intercontact between CeO<sub>2</sub> and Bi<sub>2</sub>O<sub>3</sub> reduced the Fermi level and overall E<sub>g</sub> (Fig. S19), indicating a built-in electric field formation. To further understand the separation and migration of electron-hole pairs, the surface charge density of Bi/Ce<sub>0.43</sub> heterojunction catalyst was calculated using VASP with Perdew–Burke–Ernzerhof (PBE) functional within generalized gradient approximation (GGA) and projector augmented-wave pseudopotential (PAW). The heterojunction system is constructed by the interface of (1 1 1) plane of CeO<sub>2</sub> with (1 2 0) plane of Bi<sub>2</sub>O<sub>3</sub>. Based on the optimized structure, the charge density difference was shown in Fig. 7d with the depletion of electrons (cyan colors) and accumulation of electrons (yellow color). It can be obtained from Fig. 7d that the electrons could accumulate between the heterojunction interface, suggesting a strong



interface interaction of the heterojunction along with the built-in electric field. In addition, it was found that the electrons mainly accumulate in the  $\text{CeO}_2$ , and the holes accumulate in the  $\text{Bi}_2\text{O}_3$ , indicating the electrons transfer from  $\text{Bi}_2\text{O}_3$  to  $\text{CeO}_2$ . Accordingly, the proposed mechanism for PFOA destruction by AP-Bi/Ce<sub>0.43</sub> is depicted in Fig. 7e.

The XPS analysis results showed that the  $\text{O}_\text{V}$  formed in the heterojunction of Bi/Ce<sub>0.43</sub> causes ohmic contact between  $\text{Bi}_2\text{O}_3$  and  $\text{CeO}_2$ . This heterojunction ohmic contact could enhance the pseudo-photocatalysis for spatial  $\text{e}^-/\text{h}^+$  separation and improve the charge transfer performance, as shown in the PL and TRPL analysis results.

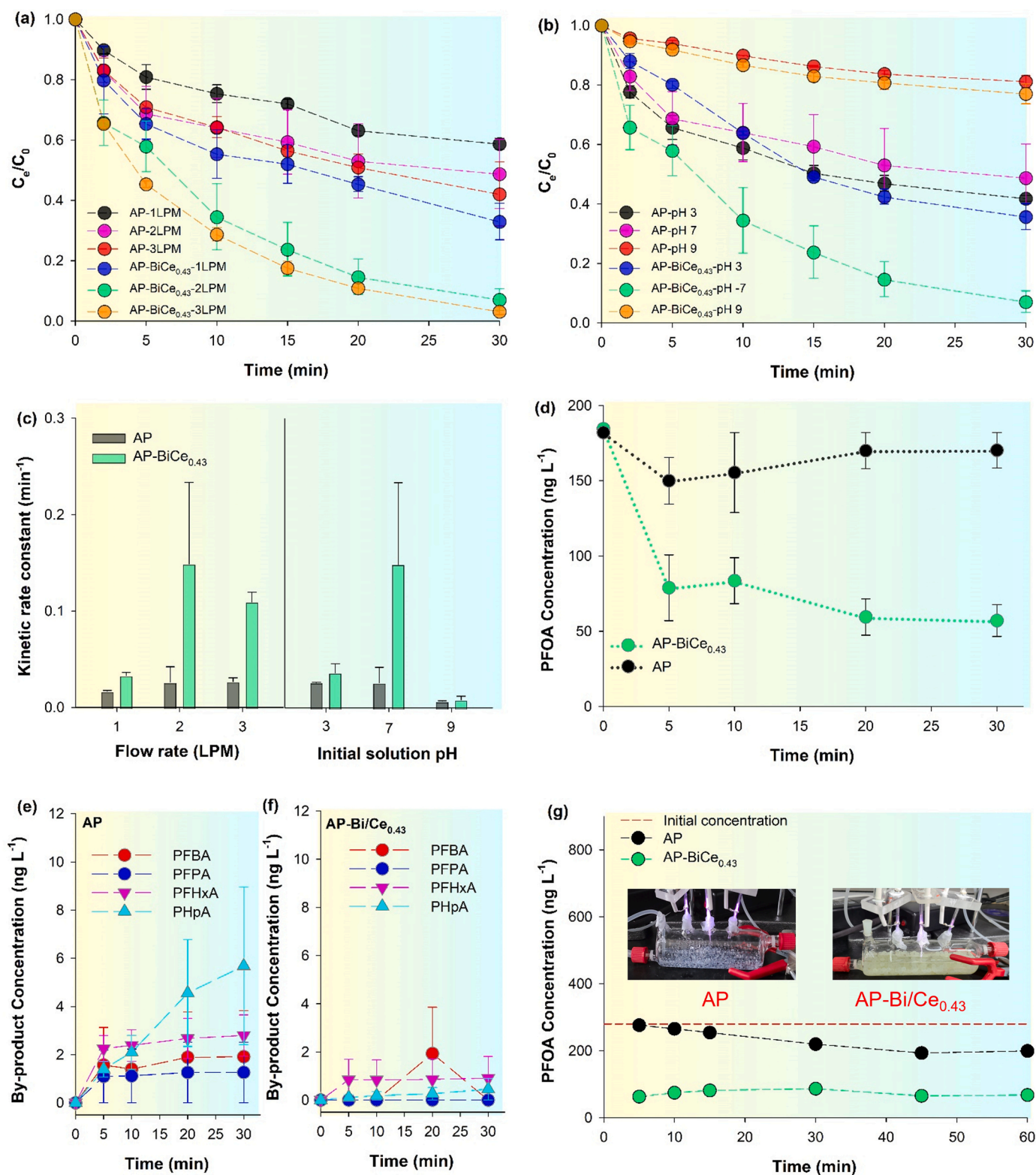


Fig. 8. Kinetic experiment and calculated kinetic rate constant for the effect of flowrate (a,c) and solution pH (b,d) for PFOA removal under AP and AP-Bi/Ce<sub>0.43</sub>. PFOA removal experiments with low initial concentration (d) and the formation of PFOA by-product (e-f) using AP and AP-Bi/Ce<sub>0.43</sub>. Continuous flow experiments for 3 jet Ar plasma systems for PFOA removal (g).

Under AP, pseudo-photocatalysis excites electron flow from Bi<sub>2</sub>O<sub>3</sub> toward CeO<sub>2</sub> due to the built-in electric field governed by O<sub>V</sub> based on the XPS, XAS, and DFT modeling results. The O<sub>V</sub> acts as an electron mediator for trapping e<sup>-</sup> and reducing its recombination with the photoexcited h<sup>+</sup>. This phenomenon can induce higher ·OH and e<sub>aq</sub><sup>-</sup> production for effective PFOA destruction, as shown by the quenching and ESR results. Therefore, introducing the built-in electric field strategy on AP catalysts for stimulating ·OH and e<sub>aq</sub><sup>-</sup> production could significantly improve PFOA destruction.

### 3.4. Ar gas flowrate and solution pH effect on PFOA removal

PFOA removal kinetics using an Ar gas flow rate of 1–3 L/min was conducted to determine the optimum Ar gas flow rate in AP. The effect of the solution pH on PFOA destruction using AP and AP-Bi/Ce<sub>0.43</sub> was also investigated. Increasing the Ar gas flow rate from 1 to 2 L/min enhanced the PFOA destruction rate (Fig. 8a and c) and defluorination performance (Fig. S20) in the absence or presence of Bi/Ce<sub>0.43</sub>. This result indicates that collisions between Ar gas molecules and plasma electrons occur more frequently as the Ar gas flow rate increases. Meanwhile, the increase in Ar gas flow rate led to the increased formation of H<sub>2</sub>O<sub>2</sub> and O<sub>3</sub> in the presence or absence of Bi/Ce<sub>0.43</sub> (Fig. S21). However, the Ar gas flow rate of 3 L/min made an insignificant difference in PFOA destruction performance compared to 2 L/min. This was because the H<sub>2</sub>O<sub>2</sub> and O<sub>3</sub> formation at 3 L/min was slightly higher than at 2 L/min in the presence or absence of Bi/Ce<sub>0.43</sub>. Generally, a high Ar gas flow rate in the jet plasma could reduce the contact time between Ar gas and turbulent flow between the plasma plume and liquid interface, thereby suppressing ROS formation. Therefore, the Ar gas flow rate of 2 L/min in AP-Bi/Ce<sub>0.43</sub> was determined to be the optimum condition for PFOA removal.

Meanwhile, AP or AP-Bi/Ce<sub>0.43</sub> exhibited the fastest PFOA removal and defluorination performance (Fig. S22) at pH 7, followed by pH 3 and 9 (Fig. 8b). In particular, the PFOA removal rates and H<sub>2</sub>O<sub>2</sub>/O<sub>3</sub> concentrations were lower at pH 9 than at pH 3 and 7 owing to the O<sub>3</sub> and ·OH consumption at high solution pH, as shown in Eqs. (3–4) (Fig. S23) [40].



In addition, AP exhibited relatively low H<sub>2</sub>O<sub>2</sub> and O<sub>3</sub> concentrations at pH 3, revealing a relatively high O<sub>3</sub>/H<sub>2</sub>O<sub>2</sub> conversion to ·OH at low solution pH. Therefore, the pH 3 solution could yield more optimized PFOA removal than pH 9. PFOA removal by AP achieved optimum conditions at pH 7 because of the highest formation of H<sub>2</sub>O<sub>2</sub>. In contrast, AP-Bi/Ce<sub>0.43</sub> yielded the lowest H<sub>2</sub>O<sub>2</sub> and O<sub>3</sub> formation but the fastest PFOA removal. Accordingly, the Bi/Ce<sub>0.43</sub> surface could form Me-OH<sub>2</sub><sup>+</sup> at pH 7 (> pH<sub>ZPC</sub>) and attract O<sub>3</sub> via electrostatic forces or hydrogen bonds, thus further favorably producing intermediate species (·OH<sub>3</sub>) and decomposing into ·OH [41].

**Table 1**  
Energy consumption comparison for PFOA removal.

System	Treatment vol (mL)	PFOA initial (mg L <sup>-1</sup> )	Treatment time (min)	Average power (W)	G50 (mg kW <sup>-1</sup> )	EEO (kW mg <sup>-1</sup> )	Ref
7-wires' DC plasma reactor	170	41.1	300	10	0.23	26.57	[42]
Hollow electrode' AC plasma reactor	15	41.1	30	7	78	0.896	[42]
Self-pulsing discharge (SPD) plasma reactor	15	41.1	30	19	87.4	0.797	[42]
DC plasma/O <sub>2</sub>	20	41.1	180	32	33.6	2.048	[43]
DC plasma/Ar	200	44.9	140	60	103.6	0.72	[44]
Plasma/MB/air	300	30	120	38.9	150.2	0.33	[45]
Electrochemical/Ti/SnO <sub>2</sub> -Sb Anode	25	50	180	-	147.1	-	[46]
Argon jet plasma	25	20	30	25	84.5	1.57	This study
Bi/Ce <sub>0.43</sub> /Argon jet plasma	25	20	30	25	480	0.43	This study

### 3.5. Energy consumption and by-products analysis

The energy consumption, such as E<sub>EO</sub> and G<sub>50</sub> for AP or AP-Bi/Ce<sub>0.43</sub>, were calculated and compared with other reported plasma studies for PFOA removal in Table 1. The E<sub>EO</sub> and G<sub>50</sub> values obtained during the PFOA removal were 1.57 kW mg<sup>-1</sup> and 84.5 mg kW<sup>-1</sup> for AP, respectively. Furthermore, the addition of Bi/Ce<sub>0.43</sub> to AP significantly improved the energy consumption (E<sub>EO</sub>, 0.43 kW mg<sup>-1</sup>) compared to other studies (0.72 ~ 26.57 kW mg<sup>-1</sup>). Notably, the G<sub>50</sub> (480 mg kW<sup>-1</sup>) of AP-Bi/Ce<sub>0.43</sub> for PFOA removal was 3.19–2086.9 times higher than that of other reported plasma systems, revealing that AP-Bi/Ce<sub>0.43</sub> exhibited considerably higher energy efficiency for PFOA removal.

Furthermore, PFOA removal kinetics at an extremely low level (180 ng L<sup>-1</sup>) were conducted to investigate the application potential of AP-Bi/Ce<sub>0.43</sub> (Fig. 8d). As a result, 7.7% and 69.1% of PFOA were removed by AP and AP-Bi/Ce<sub>0.43</sub>, respectively, within 30 min. Interestingly, AP-Bi/Ce<sub>0.43</sub> rapidly reduced the PFOA concentration below 70 ng L<sup>-1</sup> (EPA and Korean regulation) within 10 min. This result suggests that AP-Bi/Ce<sub>0.43</sub> exhibits high application potential even at extremely low PFOA concentrations. In addition, the by-products of PFOA destruction are also shown in Fig. 8e and f. PFBA, PFPA, PFHxA, and PhPA, the by-products of PFOA, were detected within the range of 1.2–6 ng L<sup>-1</sup> with AP and were measured to be < 2 ng L<sup>-1</sup> with AP-Bi/Ce<sub>0.43</sub>. This result indicates that the addition of the catalyst to AP could significantly enhance the PFOA destruction performance.

Furthermore, PFOA destruction by AP-Bi/Ce<sub>0.43</sub> with two different initial concentrations (180 and 380 ng L<sup>-1</sup>) is compared in Fig. S24. With a high initial PFOA concentration (380 ng L<sup>-1</sup>), more than ten times higher concentrations (< 26 ng L<sup>-1</sup>) of by-products were detected in 30 min compared to those (< 2 ng L<sup>-1</sup>) with 180 ng L<sup>-1</sup>. Therefore, a longer treatment time might be required to reduce by-product formation at a high initial PFOA concentration. In addition, to investigate the AP-Bi/Ce<sub>0.43</sub> applicability for another type of PFAS removal, PFOS removal was conducted. AP-Bi/Ce<sub>0.43</sub> exhibits 0.13 and 0.308 min<sup>-1</sup> PFOS removal kinetic rate constants for PFOS spiked DI and actual wastewater (Fig. S25), revealing that AP-Bi/Ce<sub>0.43</sub> is effective for the removal of PFOA and PFOS-containing wastewater.

### 3.6. Continuous flow experiments

CFEs were conducted to investigate the actual water treatment applications of Bi/Ce<sub>0.43</sub> in the continuous flow mode. Before running the CFEs, three cycles of reusability tests showed that AP-G-Bi/Ce<sub>0.43</sub> yielded 3.9–4.8 times higher PFOA removal rate for three cycles than the sole AP, indicating the high stability of G-Bi/Ce<sub>0.43</sub> (Fig. S26). To further confirm the stability of Bi/Ce<sub>0.43</sub>, XRD and XPS analysis were conducted for fresh and used catalyst. XRD analysis showed insignificant differences in the peak positions of Bi/Ce<sub>0.43</sub> before and after the PFOA removal experiments (Fig. S27). In addition, the XPS results showed that the O<sub>V</sub> percentage in Bi/Ce<sub>0.43</sub> decreased slightly from 40.7% to 39.1% after the PFOA removal tests. In comparison, the Ce(III) percentage significantly decreased from 25.9% to 17.9%, owing to the reaction with

O<sub>3</sub> produced by AP (Fig. S28 and Table S9) [47]. Based on the O<sub>V</sub> and XRD results, we can conclude that Bi/Ce<sub>0.43</sub> remained stable after the PFOA experiments. Furthermore, with a retention time of 15 min in CFEs, AP-G-Bi/Ce<sub>0.43</sub> exhibited a constant PFOA removal percentage of ~77% for 1 h, whereas only AP (with pristine glass beads) yielded a considerably lower removal rate (~28%) (Fig. 8g). The CFE results suggest that AP-G-Bi/Ce<sub>0.43</sub> could be effectively applied to PFOA removal, even at a fast continuous flow mode.

#### 4. Conclusion

In summary, we synthesized Bi/Ce composites via facile single-step calcination and applied them as catalysts in AP to boost PFOA destruction. As a result, the optimum ratio of 30% CeO<sub>2</sub> composited with Bi<sub>2</sub>O<sub>3</sub> (Bi/Ce<sub>0.43</sub>) exhibited a high SF (4.2) for PFOA destruction in AP, whereas no enhancement was observed with pristine CeO<sub>2</sub> or Bi<sub>2</sub>O<sub>3</sub>. Quenching and ESR spin-trap analysis results revealed that higher ·OH and e<sub>aq</sub> densities generated in AP-Bi/Ce<sub>0.43</sub> could increase the PFOA removal rate. A strong linear correlation was identified between the O<sub>V</sub> percentages and PFOA removal kinetic rates. Based on PEC analysis, the O<sub>V</sub> formation in the Bi/Ce composite caused a reduction in E<sub>g</sub> and an improvement in the charge transfer efficiency, resulting in the ease of high electron excitation in pseudo-photocatalysis. The heterostructure interface between Bi<sub>2</sub>O<sub>3</sub> and CeO<sub>2</sub> triggers a built-in electric field to promote the internal electron transfer and electron-rich CeO<sub>2</sub> zone, as shown in the XAS analysis, and DFT calculation results. The CFE results illustrated the scalability of AP-Bi/Ce<sub>0.43</sub> for PFAS destruction. This study demonstrates a strategy for improving the interfacial charge transfer effect in heterojunction catalysts in AP-induced pseudo-photocatalysis and shows great potential for plasma catalysis-related applications.

#### CRedit authorship contribution statement

**Choe Earn Choong:** Methodology, Validation, Investigation, Writing – original draft, Visualization. **Minhee Kim:** Methodology, Resources. **Jun Sup Im:** Resources, Validation. **Young June Hong:** Resources, Validation. **Geon Joon Lee:** Resources, Validation. **Keun Hwa Chae:** Investigation, Validation. **In Wook Nah:** Resources, Validation. **Eun Ha Choi:** Conceptualization, Investigation, Funding acquisition. **Yeomin Yoon:** Conceptualization, Validation. **Min Jang:** Writing – review & editing, Supervision, Project administration, Funding acquisition.

#### Declaration of Competing Interest

The authors declare that they have no known competing financial interests or personal relationships that could have appeared to influence the work reported in this paper.

#### Data Availability

Data will be made available on request.

#### Acknowledgment

This work was supported by the National Research Foundation of Korea (NRF) grant funded by the Korea Government (Grant No. 2021R1A6A1A03038785, 2023R1A2C1003464 and RS-2023-00240726).

#### Appendix A. Supporting information

Supplementary data associated with this article can be found in the online version at [doi:10.1016/j.apcatb.2023.123403](https://doi.org/10.1016/j.apcatb.2023.123403).

#### References

- [1] A. Cordner, V.Y. De La Rosa, L.A. Schaidler, R.A. Rudel, L. Richter, P. Brown, Guideline levels for PFOA and PFOS in drinking water: the role of scientific uncertainty, risk assessment decisions, and social factors, *J. Expo. Sci. Environ. Epidemiol.* 29 (2019) 157–171.
- [2] S.E. Fenton, A. Ducatman, A. Boobis, J.C. DeWitt, C. Lau, C. Ng, J.S. Smith, S. M. Roberts, Per- and polyfluoroalkyl substance toxicity and human health review: current state of knowledge and strategies for informing future research, *Environ. Toxicol. Chem.* 40 (2021) 606–630.
- [3] P.M.K. Reddy, C. Subrahmanyam, Green approach for wastewater treatment—degradation and mineralization of aqueous organic pollutants by discharge plasma, *Ind. Eng. Chem. Res.* 51 (2012) 11097–11103.
- [4] A. Sakudo, Y. Yagyu, T. Onodera, Disinfection and sterilization using plasma technology: fundamentals and future perspectives for biological applications, *Int. J. Mol. Sci.* 20 (2019) 5216.
- [5] S. Mededovic Thagard, G.R. Stratton, F. Dai, C.L. Bellona, T.M. Holsen, D.G. Bohl, E. Paek, E.R.V. Dickenson, Plasma-based water treatment: development of a general mechanistic model to estimate the treatability of different types of contaminants, *J. Phys. D Appl. Phys.* 50 (2016), 014003.
- [6] S. Chen, H. Wang, M. Shi, H. Ye, Z. Wu, Deep oxidation of NO by a hybrid system of plasma–N-type semiconductors: high-energy electron-activated “pseudo photocatalysis” behavior, *Environ. Sci. Technol.* 52 (2018) 8568–8577.
- [7] H. Li, Y. Sun, B. Cai, S. Gan, D. Han, L. Niu, T. Wu, Hierarchically Z-scheme photocatalyst of Ag@AgCl decorated on BiVO<sub>4</sub> (040) with enhancing photoelectrochemical and photocatalytic performance, *Applied Catalysis B: Environmental* 170–171 (2015) 206–214.
- [8] X. Yu, X. Huang, Y. Huang, Q. Feng, W. Chen, C. Ju, Y. Du, T. Bai, D. Wang, Crystal phase transition of β-Bi<sub>2</sub>O<sub>3</sub> and its enhanced photocatalytic activities for tetracycline hydrochloride, *Colloids Surf. A Physicochem. Eng. Asp.* 626 (2021), 127068.
- [9] T. Jiang, Y. Wang, Z. Guo, H. Luo, C. Zhan, Y. Wang, Z. Wang, F. Jiang, H. Chen, Bi<sub>2</sub>FeO<sub>4</sub>/Bi<sub>2</sub>O<sub>2</sub>CO<sub>3</sub> piezoelectric catalyst with built-in electric fields that was prepared via photochemical self-etching of Bi<sub>2</sub>FeO<sub>4</sub> for 4-chlorophenol degradation, *J. Clean. Prod.* 341 (2022), 130908.
- [10] T. Naganuma, E. Traversa, Stability of the Ce<sup>3+</sup> valence state in cerium oxide nanoparticle layers, *Nanoscale* 4 (2012) 4950–4953.
- [11] L. Bourja, B. Bakiz, A. Benlhamchi, M. Ezahri, S. Villain, O. Crosnier, C. Favotto, J.-R. Gavarri, Structural, microstructural and surface properties of a specific CeO<sub>2</sub>-Bi<sub>2</sub>O<sub>3</sub> multiphase system obtained at 600°C, *J. Solid State Chem.* 184 (2011) 608–614.
- [12] S. Zhang, J. Zhang, J. Sun, Z. Tang, Capillary microphotoreactor packed with TiO<sub>2</sub>-coated glass beads: an efficient tool for photocatalytic reaction, *Chem. Eng. Process. Process. Intensif.* 147 (2020), 107746.
- [13] A. Folli, S.B. Campbell, J.A. Anderson, D.E. Macphree, Role of TiO<sub>2</sub> surface hydration on NO oxidation photo-activity, *J. Photochem. Photobiol. A Chem.* 220 (2011) 85–93.
- [14] J.S. Lim, R.H. Kim, Y.J. Hong, P. Lamichhane, B.C. Adhikari, J. Choi, E.H. Choi, Interactions between atmospheric pressure plasma jet and deionized water surface, *Results Phys.* 19 (2020), 103569.
- [15] M. Wang, S. Qiu, H. Yang, Y. Huang, L. Dai, B. Zhang, J. Zou, Spectrophotometric determination of hydrogen peroxide in water with peroxidase-catalyzed oxidation of potassium iodide and its applications to hydroxylamine-involved Fenton and Fenton-like systems, *Chemosphere* 270 (2021), 129448.
- [16] H. Bader, J. Hoigné, Determination of ozone in water by the indigo method, *Water Res.* 15 (1981) 449–456.
- [17] K.R.B. Singh, V. Nayak, T. Sarkar, R.P. Singh, Cerium oxide nanoparticles: properties, biosynthesis and biomedical application, *RSC Adv.* 10 (2020) 27194–27214.
- [18] K.K. Bera, R. Majumdar, M. Chakraborty, S.K. Bhattacharya, Phase control synthesis of α, β and α/β Bi<sub>2</sub>O<sub>3</sub> heterojunction with enhanced and synergistic photocatalytic activity on degradation of toxic dye, Rhodamine-B under natural sunlight, *J. Hazard. Mater.* 352 (2018) 182–191.
- [19] H. Mou, C. Song, Y. Zhou, B. Zhang, D. Wang, Design and synthesis of porous Ag/ZnO nanosheets assemblies as super photocatalysts for enhanced visible-light degradation of 4-nitrophenol and hydrogen evolution, *Appl. Catal. B Environ.* 221 (2018) 565–573.
- [20] P. Khakbaz, F. Driussi, P. Giannozzi, A. Gambi, D. Lizzit, D. Esseni, Engineering of metal-MoS<sub>2</sub> contacts to overcome Fermi level pinning, *Solid-State Electron.* 194 (2022), 108378.
- [21] C.E. Choong, C.M. Park, Y.-Y. Chang, J.R. J.-k. Yang, S.-E. Kim, B.-H. Oh, E. H. Jeon, Y. Choi, M. Yoon, Jang, Interfacial coupling perovskite CeFeO<sub>3</sub> on layered graphitic carbon nitride as a multifunctional Z-scheme photocatalyst for boosting nitrogen fixation and organic pollutants demineralization, *Chem. Eng. J.* 427 (2022), 131406.
- [22] F.A. Hussain, S.E. Janisse, M.C. Heffern, M. Kinyua, J.M. Velázquez, Adsorption of perfluorooctanoic acid from water by pH-modulated Brønsted acid and base sites in mesoporous hafnium oxide ceramics, *iScience*, 25 (2022) 104138.
- [23] L. Fijolek, L. Wolski, Bifunctional CePO<sub>4</sub>/CeO<sub>2</sub> nanocomposite as a promising heterogeneous catalyst for the enhancement of the ozonation recovery effect in the presence of chloride ions, *Sci. Rep.* 12 (2022) 9043.
- [24] M. Smith, L. Scudiero, J. Espinal, J.-S. McEwen, M. Garcia-Perez, Improving the deconvolution and interpretation of XPS spectra from chars by ab initio calculations, *Carbon* 110 (2016) 155–171.
- [25] A.B. Haruna, P. Mwonga, D. Barrett, C.B. Rodella, R.P. Forbes, A. Venter, Z. Sentsho, P.J. Fletcher, F. Marken, K.I. Ozoemena, Defect-engineered β-MnO<sub>2</sub>–



- precursors control the structure–property relationships in high-voltage spinel  $\text{LiMn}_{1.5}\text{Ni}_{0.5}\text{O}_{4-\delta}$ , *ACS Omega* 6 (2021) 25562–25573.
- [26] G. Zhai, S. Liu, S. Si, Y. Liu, H. Zhang, Y. Mao, M. Zhang, Z. Wang, H. Cheng, P. Wang, Z. Zheng, Y. Dai, B. Huang, Oxygen vacancies enhanced ozonation toward phenol derivatives removal over  $\text{Ov-Bi}_2\text{O}_3$ , *ACS ES&T, Water* 2 (2022) 1725–1733.
- [27] K.T. Wong, C.E. Choong, I.W. Nah, S.-H. Kim, B.-H. Jeon, Y. Yoon, E.H. Choi, M. Jang, Interfacial Schottky junctions modulated by photo-piezoelectric band bending to govern charge carrier migration for selective  $\text{H}_2\text{O}_2$  generation, *Appl. Catal. B: Environ.* 315 (2022), 121581.
- [28] J. Zhang, Z. Xiong, J. Wei, Y. Song, Y. Ren, D. Xu, B. Lai, Catalytic ozonation of penicillin G using cerium-loaded natural zeolite (CZ): Efficacy, mechanisms, pathways and toxicity assessment, *Chem. Eng. J.* 383 (2020), 123144.
- [29] J. Wang, X. Quan, S. Chen, H. Yu, G. Liu, Enhanced catalytic ozonation by highly dispersed  $\text{CeO}_2$  on carbon nanotubes for mineralization of organic pollutants, *J. Hazard. Mater.* 368 (2019) 621–629.
- [30] K.P. Madden, H. Taniguchi, The role of the DMPO-hydrated electron spin adduct in DMPO-OH spin trapping, *Free Radic. Biol. Med.* 30 (2001) 1374–1380.
- [31] K.T. Wong, S.C. Kim, K. Yun, C.E. Choong, I.W. Nah, B.-H. Jeon, Y. Yoon, M. Jang, Understanding the potential band position and  $e^-/h^+$  separation lifetime for Z-scheme and type-II heterojunction mechanisms for effective micropollutant mineralization: Comparative experimental and DFT studies, *Appl. Catal. B Environ.* 273 (2020), 119034.
- [32] T. Selvamani, S. Anandan, L. Granone, D.W. Bahnemann, M. Ashokkumar, Phase-controlled synthesis of bismuth oxide polymorphs for photocatalytic applications, *Mater. Chem. Front.* 2 (2018) 1664–1673.
- [33] W. Wang, Q. Zhu, F. Qin, Q. Dai, X. Wang, Fe doped  $\text{CeO}_2$  nanosheets as Fenton-like heterogeneous catalysts for degradation of salicylic acid, *Chem. Eng. J.* 333 (2018) 226–239.
- [34] B.S. Araújo, A.M. Arévalo-López, C.C. Santos, J.P. Attfield, C.W.A. Paschoal, A. P. Ayala, Spin–phonon coupling in monoclinic  $\text{BiCrO}_3$ , *J. Appl. Phys.* 127 (2020), 114102.
- [35] L.E. Gómez, J.F. Múnera, B.M. Sollier, E.E. Miró, A.V. Boix, Raman in situ characterization of the species present in  $\text{Co/CeO}_2$  and  $\text{Co/ZrO}_2$  catalysts during the COPrOx reaction, *Int. J. Hydrog. Energy* 41 (2016) 4993–5002.
- [36] W.-C. Wang, S.-Y. Chen, P.-A. Glans, J. Guo, R.-J. Chen, K.-W. Fong, C.-L. Chen, A. Gloter, C.-L. Chang, T.-S. Chan, J.-M. Chen, J.-F. Lee, C.-L. Dong, Towards understanding the electronic structure of Fe-doped  $\text{CeO}_2$  nanoparticles with X-ray spectroscopy, *Phys. Chem. Chem. Phys.* 15 (2013) 14701–14707.
- [37] F. Frati, M.O.J.Y. Hunault, F.M.F. de Groot, Oxygen K-edge X-ray absorption spectra, *Chem. Rev.* 120 (2020) 4056–4110.
- [38] Y. Lee, G. He, A.J. Akey, R. Si, M. Flytzani-Stephanopoulos, I.P. Herman, Raman analysis of mode softening in nanoparticle  $\text{CeO}_2-\delta$  and  $\text{Au-CeO}_2-\delta$  during CO oxidation, *J. Am. Chem. Soc.* 133 (2011) 12952–12955.
- [39] Y. Wang, J. Zhao, Y. Zhu, B. Zhou, X. Zhao, Z. Wang, Controlled fabrication and optical properties of 3D hierarchical  $\alpha\text{-Bi}_2\text{O}_3$  siamesed microflowers, *Colloids Surf. A Physicochem. Eng. Asp.* 434 (2013) 296–302.
- [40] J. Ma, M. Sui, T. Zhang, C. Guan, Effect of pH on  $\text{MnOx/GAC}$  catalyzed ozonation for degradation of nitrobenzene, *Water Res.* 39 (2005) 779–786.
- [41] P. Li, R. Miao, P. Wang, F. Sun, X.-y Li, Bi-metal oxide-modified flat-sheet ceramic membranes for catalytic ozonation of organic pollutants in wastewater treatment, *Chem. Eng. J.* 426 (2021), 131263.
- [42] M. Saleem, O. Biondo, G. Sretenović, G. Tomei, M. Magarotto, D. Pavarin, E. Marotta, C. Paradisi, Comparative performance assessment of plasma reactors for the treatment of PFOA; reactor design, kinetics, mineralization and energy yield, *Chem. Eng. J.* 382 (2020), 123031.
- [43] R. Hayashi, H. Obo, N. Takeuchi, K. Yasuoka, Decomposition of perfluorinated compounds in water by DC plasma within oxygen bubbles, *Electr. Eng. Jpn.* 190 (2015) 9–16.
- [44] H. Obo, N. Takeuchi, K. Yasuoka, Decomposition of perfluorooctanoic acid in water using multiple plasma generation, *IEEE Trans. Plasma Sci.* 41 (2013) 3634–3639.
- [45] H. Zhang, P. Li, A. Zhang, Z. Sun, J. Liu, P. Héroux, Y. Liu, Enhancing interface reactions by introducing microbubbles into a plasma treatment process for efficient decomposition of PFOA, *Environ. Sci. Technol.* 55 (2021) 16067–16077.
- [46] Q. Zhuo, S. Deng, B. Yang, J. Huang, G. Yu, Efficient electrochemical oxidation of perfluorooctanoate using a  $\text{Ti/SnO}_2\text{-Sb-Bi}$  anode, *Environ. Sci. Technol.* 45 (2011) 2973–2979.
- [47] H. Wang, S. Luo, M. Zhang, W. Liu, X. Wu, S. Liu, Roles of oxygen vacancy and  $\text{Ox-}$  in oxidation reactions over  $\text{CeO}_2$  and  $\text{Ag/CeO}_2$  nanorod model catalysts, *J. Catal.* 368 (2018) 365–378.